PRECISION ENGINEERING CENTER

2008 INTERIM REPORT
September 2008

Sponsors:

B & W Y-12
Lexmark International, Inc.
Lockheed Martin Corporation
Minnesota Mining & Manufacturing Company
National Science Foundation
Panasonic Technologies, Inc.
Vistakon Division of Johnson & Johnson Vision Care Inc.

Faculty:

Thomas Dow, Editor
Ronald Scattergood
Jeffrey Eischen
David Youden

Graduate Students:

David Brehl
Qunyi Chen
Stephen Furst
Brandon Lane
Erik Zdanowicz

Summer Students:

Jacob Galloway
Walter Bright

Staff:

Kenneth Garrard
Alexander Sohn
Paula Kelley

Consultants:

Karl J. Falter
Amir Pirzadeh, Tisfoon Ulterior Systems

TABLE OF CONTENTS

1 FAST LONG RANGE ACTUATOR (FLORA)

Qunyi Chen
Graduate Student
Thomas A. Dow
Dean F. Duncan Distinguished Professor
Department of Mechanical and Aerospace Engineering
Kenneth Garrard and Alex Sohn
Precision Engineering Center Staff

1.1 INTRODUCTION

The development of a Fast LOng Range Actuator (FLORA) is driven by the need to create Non-Rotationally Symmetric (NRS) optical surface with millimeters of sag at high production rates, since the existing technology on tool positioning with the PZT FTS is limited by stroke or the slow slide servo is limited by speed. The FLORA piston is supported by an air bearing, driven by a linear motor, measured by a high-resolution linear encoder and controlled by a high-speed DSP based controller. To retain the surface quality of existing diamond turning machines (less than 5 nm RMS surface finish, less than 150 nm form error), the real-time tool motion control must position the tool within ±20 nm of desired location while moving the tool over a range of 4 mm at a frequency of 20 Hz in the machining process. The requirements on the motion range (4 mm), speed (250 mm/s) and positioning error (30 nm) make the control of tool motion very demanding. The key parameters that set this application apart are the ratio of range to position error (130,000) and the position error to speed (120 ns).

1.2 SYSTEM DEVELOPMENT

A prototype FLORA was built in 2004 and has been upgraded over the last two years with support from NSF. A photograph of the actuator is shown in Figure 1. The FLORA consists of a light-weight, aluminum-honeycomb triangular piston, an orifice air bearing, an ironless three-phase linear motor, a linear amplifier and a laser linear encoder. This physical construction of actuator is free of major nonlinearities such as hysteresis, backlash and friction commonly seen in other motion

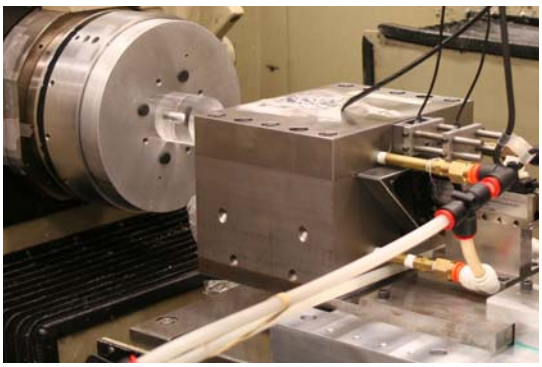

Figure 1. Photograph of the FLORA system mounted on the ASG 2500 DTM.

systems. When integrated with high-speed (20 kHz sampling rate) and high-bandwidth real time closed-loop control, the FLORA exhibited good tool motion control and machining performance.

1.3 METROLOGY

To create freeform surface, the position of the tool is synchronized to the position of the DTM axes by generating its motion command (***Z***) as a function of the spindle angular position (***θ***), z-slide position ($\boldsymbol{Z_s}$) and cross-feed slide position (***X***) in Equation (1).

$$Z = f(X, Z_s, \theta) \tag{1}$$

It is desirable to have any measurement induced tool positioning error within a few nanometers. Laser interferometers installed on the ASG-2500 have measurement resolution below 2 nm for z-slide and x-slide position. However, there are various measurement errors in the other two motion axes.

1.3.1 SPINDLE ANGULAR POSITION MEASUREMENT

A 20,000 count/rev encoder (Heidenhain ERO1324) is used for spindle angular position measurement. In addition to the limited angular encoder resolution issue [1], the encoder alignment also contributes to the errors in the tool motion trajectory. The runout in the encoder disk will appear as a non-uniform pitch of the angular steps when read by the stationary read head. Because the rotary error repeats each revolution and the spindle speed is constant over that short interval, this measurement error is calibrated and compensated at the servo sampling rate. The effectiveness of these techniques was experimentally verified using a tilted flat.

1.3.2 TOOL POSITON MEASUREMENT

The tool position is measured by a linear encoder (Sony BH25) with 0.25 μm signal wave length. It is one of the best reflective type linear encoders available. Once integrated with PMDi interpolator, the position measurement shows 3 nm of noise when the air bearing is turned off and the piston maintains static position. However, the position measurement resolution degrades to 125 nm [1] when the sin/cos encoder signals entering the interpolator reach its frequency limit of 325 kHz. Figure 2(a) shows the error that occurs when the encoder frequency exceeds the interpolator limit. The interpolator ceases to operate and the encoder resolution increases to zero crossing of the sine wave of 125 nm (half the scale period of 250 nm). To addresses this problem, collaborative efforts with PMDi were taken to increase the frequency limit of interpolation process above 1 MHz. This is the sine wave frequency for the peak speed of the ± 2 mm, 20 Hz sine wave or 250 mm/sec. The steps were:

(1) Remove signal filtering and compensation in interpolation process,

(2) Synchronize the analog interpolation and digital zero-crossings counting paths ,

(3) Make 4x interpolation of 10 MHz ADC at 40 MHz clock cycle.

Figure 2(b) shows the position error for 2 mm 20 Hz sine wave tracking with a PID controller and an acceleration feedforward controller, the improvement on the motion control quality is obvious by comparing the plots in [1].

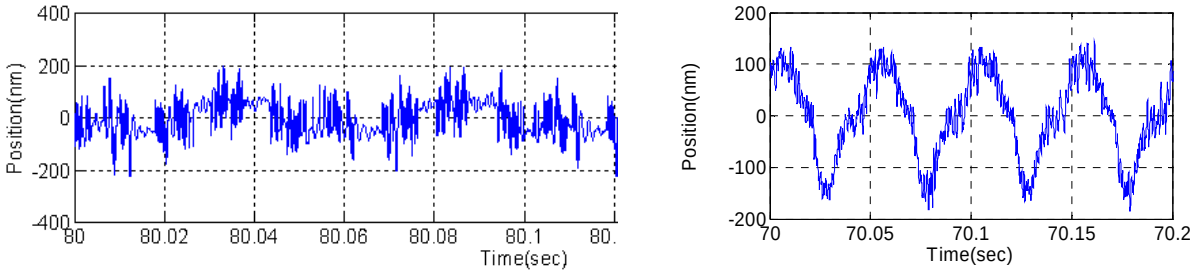

(a) (b)

Figure 2. 2 mm 20 Hz sinusoidal tracking test. (a) shows the error when the sine wave frequency exceeds the interpolator speed and (b) tracking error with high-speed interpolator.

1.4 CONTROL SYSTEM DESIGN

The functional requirement for the FLORA is to follow the tool motion profile as closely as possible while minimizing the effects of measurement errors and disturbances. The disturbance force to the tool motion could be from the errors in motor actuation force generation process, or from the tool-workpiece interaction process which largely depends on the tool wear condition, and the material properties of the workpiece. Figure 3 shows a block diagram of the proposed composite controller structure to achieve control task. A position feedback controller (K_{POS}) is designed based on the dominant linear model to establish the basic closed-loop control system. A feedforward controller (K_{FF}) is applied to compensate the phase lag in profile tracking. A disturbance observer (*DOB*) improves the disturbance rejection in the low frequency range. An adaptive feedforward controller (K_{AFC}) is designed to further improve trajectory tracking and reject disturbances at selected frequencies.

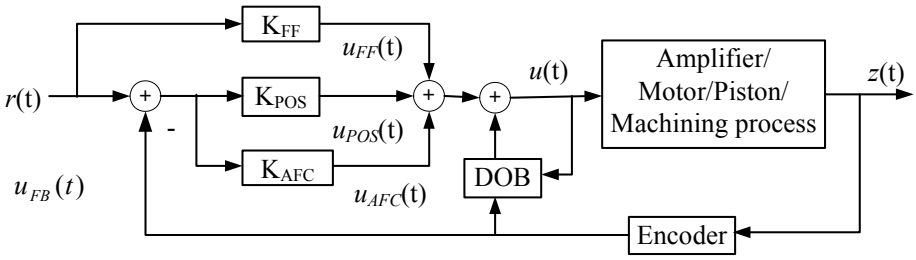

Figure 3. Schematic diagram of the proposed controller structure

1.4.1 CLASSICAL POSITION FEEDBACK CONTROLLER

Based on the measured open loop system frequency response characteristic, three different position feedback, lead-lag controllers were designed with different loop gain crossover frequencies of 100Hz, 600Hz, and 1000Hz as shown in Figure 4. The control system with 100 Hz crossover frequency has much lower peak magnitude in the sensitivity plot and has highest stability margin, but it the lowest speed of response and stiffness for the servo control. The system with 1000 Hz crossover frequency has the highest servo stiffness, but its gain margin is the lowest, it causes the saturation of the amplifier during the tracking task. One anticipated change in the system is to retune the current loop in the amplifier to increase its bandwidth. This change will allow higher gain without saturation and servo stiffness can be placed at a higher level.

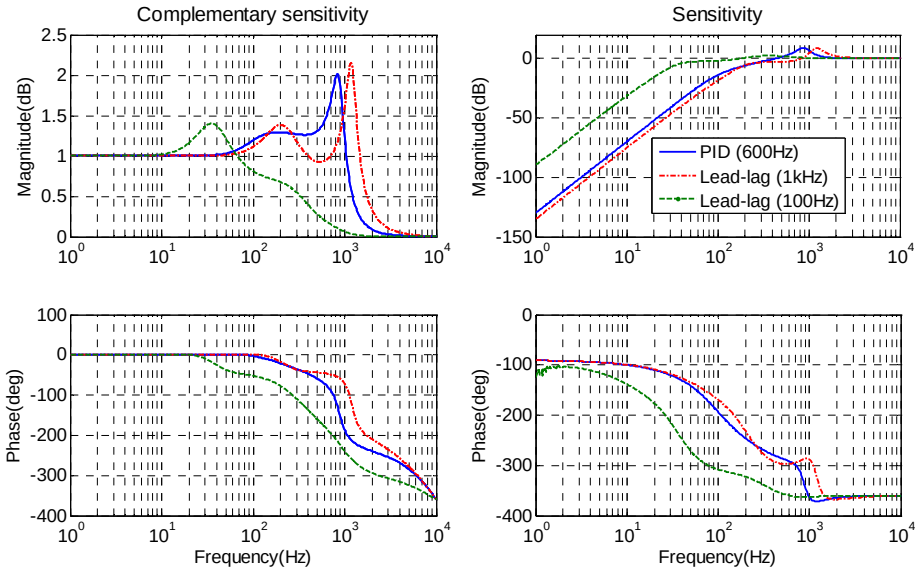

(a) Complementary sensitivity function (b) Sensitivity function

Figure 4. Closed loop simulations controllers with three different crossover frequencies

1.4.2 ADAPTIVE FEEDFORWARD CONTROLLER

Because of the speed and resolution demands in ultraprecision machining, a control system with position feedback and acceleration feedforward may not be sufficient. To improve the profile tracking and disturbance rejection, an adaptive feedforward control (AFC) approach [2] has been explored. The basic principle of this control approach is to estimate the magnitudes and phases of the position error at selected frequencies and to generate the control effort needed to remove the error at these frequencies. Functionally, it is equivalent to putting a model of the disturbance signal into the feedback control to create larger feedback gains at these selected frequencies.

The transfer function G_c from the basic position feedback controller (K_{POS}) for the open loop system G in Equation (3) is used to find the parameters for the adaptive algorithm in Equation (4) at the selected frequency, ω.

$$G_{cn}(i\omega) = A_c e^{i\phi}, \quad G_c(s) = \frac{G(s)}{1 + K_{POS} G(s)} \tag{3}$$

$$K_{AFC}(z) = \frac{2\alpha}{A_C} \frac{z^2 \cos(\phi) - z\cos(\omega T_s - \phi)}{z^2 - 2z\cos(\omega T_s) + 1} \tag{4}$$

where T_s is the sampling interval, the parameter α is a convergence coefficient, A_C and ϕ are nominal magnitude and phase derived from the frequency response of the transfer function Gc from $u_{AFC}(t)$ to $z(t)$. The controller parameter α is selected to maximize the convergence rate of the adaptive controller (shorten the transient response) while maintaining the stability (robustness) of closed-loop controller.

Figure 5 shows the positioning error in a test of sinusoidal profile tracking at the amplitude of 2 mm and the frequency of 20 Hz. A combination of PID, AFC and acceleration feedforward controller is used in this test. The frequency ω in Equation (4) was the sine wave excitation frequency (20 Hz) and the parameter α was selected as 0.001. The tracking error in Figure 5(a) is ±70 nm (only 0.0035% of the positions command) compared to ±170 nm a similar experiment without the AFC as shown in Figure 2(b). The frequency spectrum in Figure 5(b) shows the tracking error has negligible magnitude at the fundamental frequency (20 Hz) but has peaks at 2 and 3 times this frequency. For the tool motion path in the machining of typical freeform surface, only the first few harmonics of the spindle rotational frequency have significant magnitudes. The position error at these frequencies could be reduced by putting the basic element of AFC in Equation (4) in parallel with the closed loop controller.

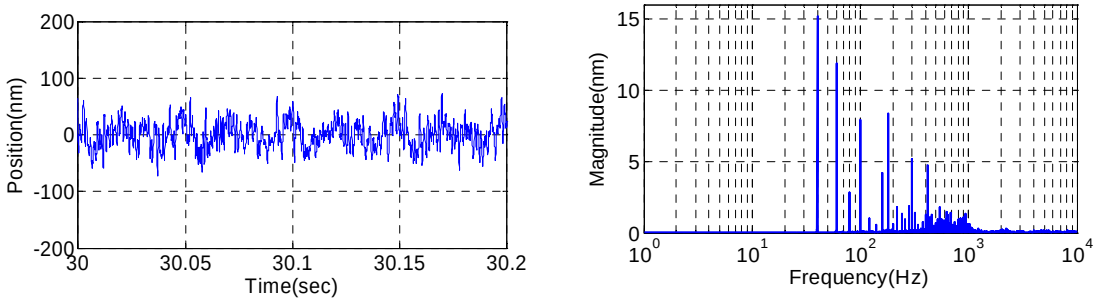

(a) (b)

Figure 5. 2mm 20 Hz sinusoidal tracking test (a) Tracking error for four motion cycles (b) Frequency spectrum of tracking error

1.4.3 FEEDFORWARD CONTROLLER

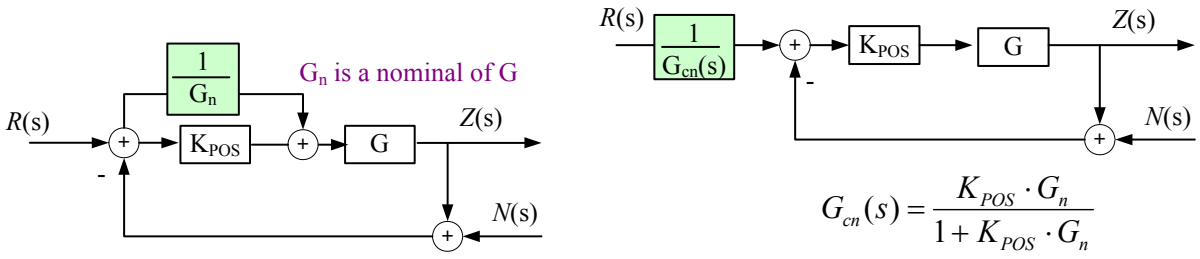

(a) (b)

Figure 6. Implementation structure of feedforward controller (a) from open loop system dynamics (b) from the closed-loop system dynamics

Most feedforward controller designs can be classified as a form of command shaping. Command shaping refers to a broad range of techniques that "shape" or design the input to achieve certain performance requirements. By processing the desired output by a feedforward controller which acts as an inverse of the open/closed loop system as shown in Figure 6, the effective bandwidth of the overall system can be improved compared with feedback alone. The acceleration feedforward controller in [1] only considers the moving mass for the open loop system dynamics. To increase the performance of a feedforward controller, a higher-order dynamics equation can be used to include both moving mass and current loop dynamics in the servo system.

1.5 CUTTING PERFORMANCE

1.5.1 FLAT

A flat surface was machined to test the ability of the FLORA piston to hold position while being excited by the machining forces. The flat was machined with a 0.53 mm radius diamond tool at 500 rpm with a 1 mm/min feedrate (2 μm/rev) and 2 μm depth of cut on the finish pass. Table 1 compares the RMS of flat surface finish when the tool is locked or positioned by the control system. For the locked case, the air bearing was locked down by removing the air from the lower sides of the triangular piston. Comparing to the case of the locked tool, the three controllers added surface roughness. The active closed-loop control adds 3.7 nm RMS error for the 100 Hz lag-lead controller, but a much larger error for higher crossover frequency controller design. The results indicate that it is desirable to remove the major peaks in the 600 Hz and 1000 Hz design (Figure 4). To maintain the speed of response and servo stiffness, it is necessary to have faster current loop dynamics control.

Table 1. Comparison of RMS error with a locked and position controlled tool holder

Unit (nm)	Tool holding method			
	Piston Locked	**Lag-lead (100 Hz)**	**PID (600 Hz)**	**Lag-lead (1 kHz)**
RMS Piston motion error	1	14.4	16.0	14.3
RMS Surface finish	3.7	7.4	11.4	10.5

1.5.2 TILTED FLAT

A tilted flat was machined to evaluate the ability of the servo to create non-rotationally symmetric optical surfaces. The tilted flat requires a sine wave motion of the tool with the amplitude changing linearly with the radius [1]. Only a combination of acceleration feedforward controller and PID controller is used for the tool motion control in tilted flat machining. Acrylic tilted flats with 50.8 mm diameter and 4 mm sag were created at three different spindle speed, 300 rpm, 600 rpm and 1200 rpm.

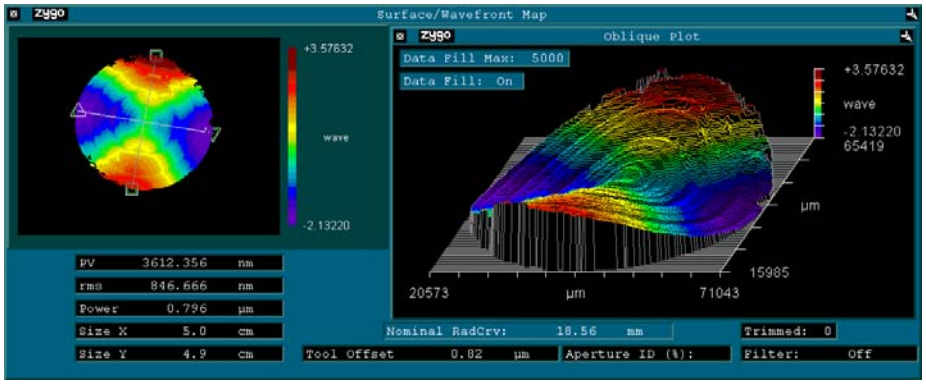

(a)

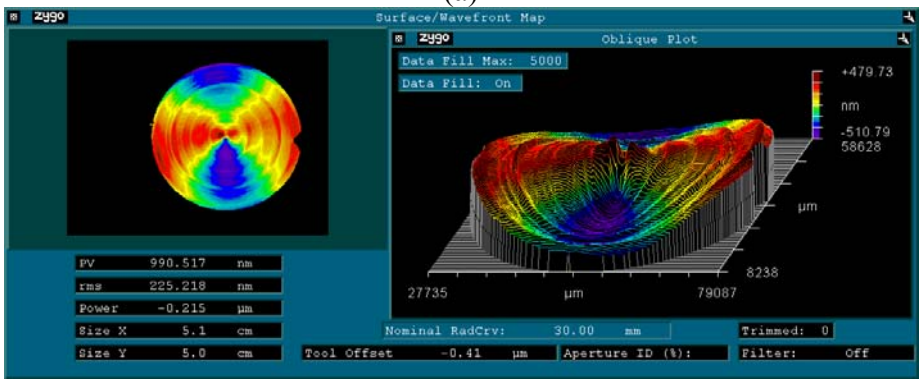

(b)

Figure 7. Measured flatness error of the 50 mm diameter tilted flat using laser interferometer (a) With spindle encoder measurement error (b) With the corrected spindle encoder reading

The measurement of flatness by the Zygo GPI laser interferometer for the tilting surface shows consistent pattern as in Figure 7(a) for the case of 600 rpm. The plot shows the surface residual error with the best-fit tilted flat removed. The flatness of the machined plastic part was 3.6 μm PP. Note that the surface has astigmatism (two highs and two lows on the surface) and the high spot of this astigmatism has about 80° lead to the high spot of the tilted flat. The 3.6 μm flatness error is mainly caused by the spindle rotary encoder feedback error due to the rotor runout as discussed in Section 3.3.1. This error introduces twice-per-spindle- revolution error in tool motion trajectory which increases in amplitude when the tool cutting depth increases. Since this error is repeatable, it was measured and removed in the motion trajectory. The effectiveness of this solution is validated in another machining test at 600 rpm, in which the flatness is reduced to less than 1 μm in Figure 7(b). The measured average surface finish is 22 nm (RMS).

1.6 CONCLUSIONS

For a DTM with FLORA, the only thing new to the process is the tool positioning. It has been proven through machining tests that the tool motion control (from encoder scale to read-head) is one of the critical factors determining the achievable surface quality. The smaller the positioning error, the smaller the surface form error and roughness. To achieve 100000: 1 tool positioning precision at a frequency of 20 Hz, it requires a systematic approach to put the performance of every system component into consideration and properly integrate them through high speed and high bandwidth real time control. The results achieved so far in the motion control and machining tests establish the base-line performance of the existing design and the new control system of FLORA but do not yet meet the ultimate goal. Future efforts will refine the system's physical design to minimize errors and disturbances, increase the current loop bandwidth, push the mechanical resonance frequency higher than 3 kHz, and implement advanced control approaches to optimize both the trajectory tracking performance and disturbance rejection performance during the machining of NRS optical surfaces.

REFERENCES

1. Chen, Qunyi, Dow, Thomas A., Garrard, Kenneth and Sohn, Alex, *Fast long range actuator – FLORA*, PEC Annual Report, Volume XXV, p35-54, 2007.
2. Messner, W. and Bodson, M., "Design of Adapative Feedwardard Algorithms using Internal Model Equivalence", International Journal of Adaptive Control and Signal Processing, Vol 9, pg 199-212m 1995.

2 DESIGN OF A FAST LONG RANGE ACTUATOR – FLORA II

Erik Zdanowicz
Graduate Student
Dr. Jeffrey Eischen
Associate Professor
Department of Mechanical and Aerospace Engineering

2.1 INTRODUCTION

The objective of this NFS sponsored research is to develop machinery to fabricate Non-Rotationally Symmetric (NRS) optical surfaces. NRS surfaces have typically been machined using very slow spindle speeds or actuators with a limited range of several hundred μm. This means only limited surface features can be machine or the process takes a long time. A Fast LOng Range Actuator (FLORA) has been constructed [1] with a goal of machining NRS surfaces with a range of motion of ± 2 mm at 20 Hz. For the surface to have the same quality as conventional diamond turning machines the surface must have a form error of less than 150 nm peak-to-valley and a surface finish of 5 nm RMS.

The FLORA system consists of a triangular aluminum honeycomb piston supported by orifice type air bearings and driven by a linear motor. While machining with FLORA was successful, the system dimensions are large when compared with the range of motion and the size of the tool and the piston weighed 650 grams. In addition, the air bearing on the FLORA has 200 nm of vertical vibration which has an impact on the surface finish possible.

A new design, FLORA II, has been created to address the limitations of its predecessor. The FLORA II package is smaller and lighter than FLORA while maintaining bearing stiffness and improving system dynamics. This was accomplished through structural analysis supplemented with experimental testing. The design described in this paper will show how the FLORA II can produce high quality NRS optical surfaces from a small, lightweight system.

2.2 AIR BEARINGS

One of the main features in the FLORA design is the air bearing. This bearing eliminates friction, supports the tool with little or no deflection and moves piston in a straight line. The

original FLORA design had an orifice-type air bearings that consist of a number of small orifices along the bearing surface to create the pressurized air film that supports the piston. It is believed that these bearings are responsible for the 200 nm vertical vibration of FLORA [1]. For this reason, FLORA II was designed with porous-carbon air bearings. Porous air bearings are constructed with an aluminum backing that acts as a manifold to distribute air through a porous carbon material. This porous carbon material has millions of small holes for air distribution and creates a nearly uniform pressure distribution over the surface of the bearing. Orifice type bearings have more pressure variation over the face of the bearing.

Finite Element Analysis (FEA) software is a powerful design tool that if used properly, can provide important information such as deformation of a complex body under load. The software ANSYS has an elastic foundation type of support which attaches a bed-of-springs from a moving part to a fixed support. This bed-of-springs foundation can be used to approximate the stiffness of the air bearing provided by the pressurized air. The company that makes the porous bearings, New Way [2], publishes an overall stiffness for their bearings at a certain pressure. To use the bed-of-springs approach, ANSYS requires specification of stiffness per unit area. Therefore, equivalent foundation stiffness had to be derived from the stiffness provided by New Way for use in the ANSYS model. To verify the model, a 25 mm diameter air bushing shown in Figure 1 was purchased. The air bushing consists of a hollow aluminum tube with the carbon bearing material on the inside. A circular shaft rides in the bearing with a radial film thickness of about 5 μm. The aluminum tube is supported by 4 O-rings and an epoxy resin is injected between the tube and housing to rigidly support the bearing.

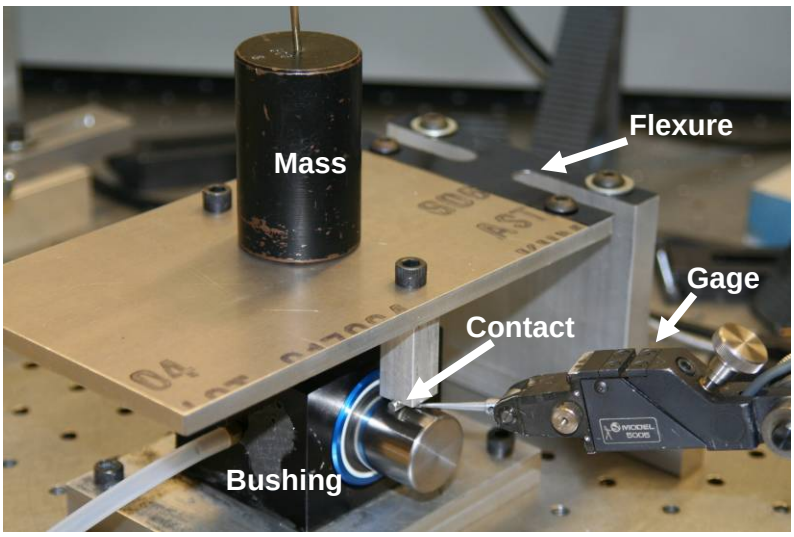

Figure 1. Radial stiffness test.

2.2.1 AIR BEARING EXPERIMENT

Static and dynamic stiffness and vibration experiments were run on the test bushing to verify the performance and the theoretical derivations of stiffness. The tests consisted of the 25 mm long carbon bearing bushing, a 110 mm long stainless steel shaft, a flexure loading device and a mounting housing.

Static Air Bearing Measurements

New Way provides two stiffness values for each bushing: radial and pitch. Radial stiffness is the load required to produce a unit value of radial translation of the shaft. Pitch is the moment required to produce a unit rotation of the shaft in the bushing. Figure 2 shows the radial and pitch directions.

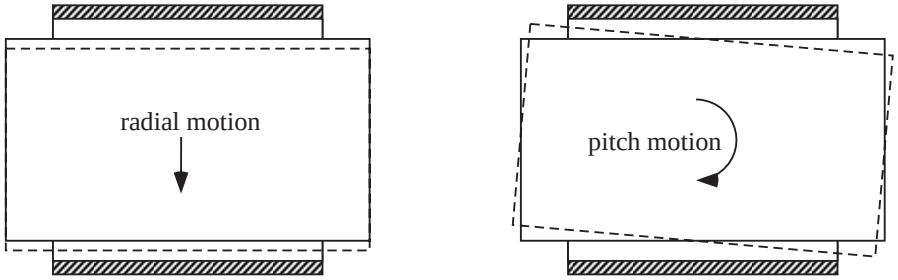

Figure 2. Radial motion is shown on the left while pitch motion is shown on the right.

The first static test was to verify the radial stiffness of the bushing. This is the stiffness of vertical translation of the shaft inside the bushing. The experiment was run as shown in Figure 1. The known mass was placed on the center of a load plate that was hinged to a vertical support by a thin flexure. The flexure had cut outs from the sides to allow the plate to twist so the contacts would apply equal loads to each end of the shaft. The contacts had small cylinders glued to the ends so as to apply a point contact. A lever-type gage head was used to measure the displacement under the contact. Three different known masses were placed on the load plate 10 times each and the displacements were recorded. From these experiments it was found that the radial stiffness was 25.8 N/μm. This value is close to the 27.9 N/μm predicted using the value (34 N/μm) [2] published by New Way reduced due to the bending stiffness of the steel shaft (156 N/μm).

To measure the pitch stiffness, the same equipment was used as in the radial test except one contact was removed to apply a moment to the bearing. The flexure shown in Figure 1 was thinned in the center to allow rotation of the loading plate. For the moment experiments, a new stiffer flexure with no cutouts was fabricated. In this experiment two gage heads, one on each

side of the bushing, were used. This orientation allowed the rotation of the shaft to be determined. The measured pitch stiffness was 5.5 N-m/milli-radian which is close to stiffness quoted by New Way of 5.3 N-m/milli-radian [2].

Dynamic Air Bearing Measurements

The two factors that were the focus of the bushings dynamics experiments were natural frequencies and noise. Natural frequencies were obtained by measuring one end of the shaft with a capacitance gage while tapping the other end of the shaft. The signal analyzer then output the natural frequencies of the shaft on the pressurized air film. The first natural frequency, a rigid body pitch mode, was observed at about 700 Hz. The results are shown in Figure 3. The top plot is the time series of the shaft motion resulting from a single tap showing a peak spacing of 1.43 msec or 700 Hz. The lower plot is the frequency spectrum of the top plot that shows peaks at 590 and 690 Hz.

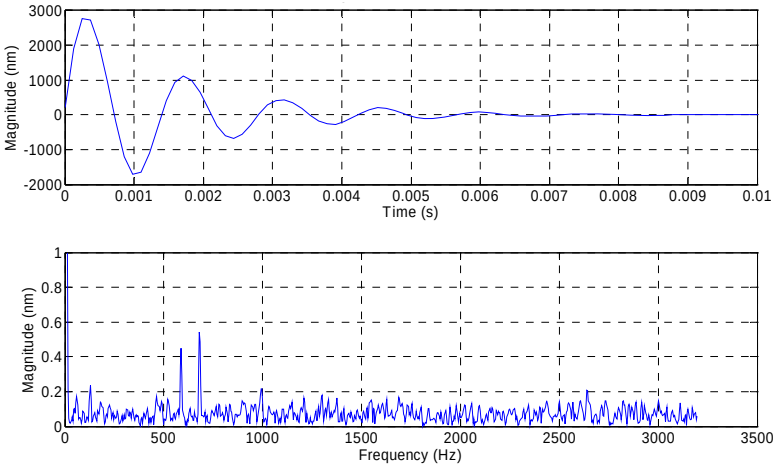

Figure 3. Vertical motion of shaft when tapped in bushing measured by a capacitance gage.

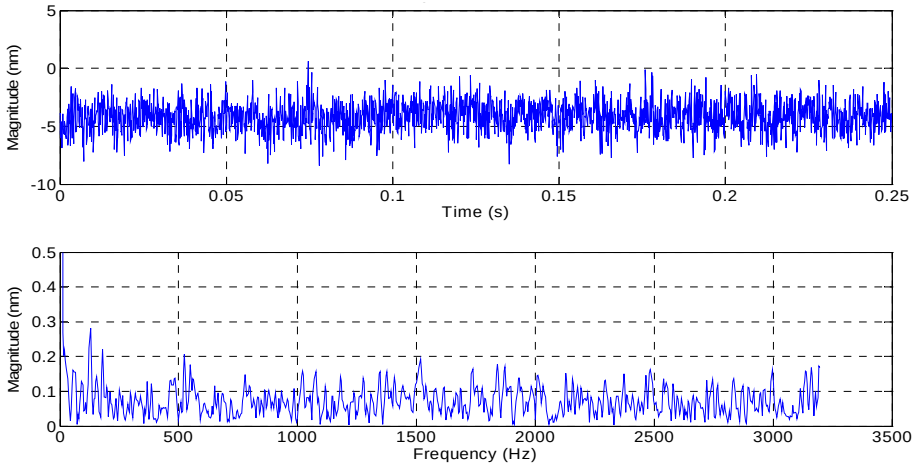

Figure 4. Steady-state vertical motion of shaft in bushing measured by a capacitance gage.

The second reason for looking at the dynamics of the bushing was to determine the steady state vertical motion of the porous type bearing compared to the current FLORA. This experiment was the same as before except there was no excitation. A baseline recording of the shaft sitting in the bearing is shown in Figure 4. Figure 4 shows that the bushing has a peak-to-peak motion of ± 4 nm. This is noise from the cap gage. Recall that FLORA had a motion of ± 100 nm which is significantly larger than the bushing. This finding reinforces the idea that porous air bearings are the right choice for use in FLORAI.

2.2.2 AIR BEARING ANALYSIS

To compare the results of the experiments and ANSYS simulations of the bearing stiffness, equivalent radial and pitch stiffness are needed. The approach that was taken for both cases was to use a bed-of-springs approximation where the air bushing is modeled as a series of springs connected the shaft to the inside the bushing.

Equivalent Radial Stiffness

It is assumed that the equivalent radial stiffness will be a function of the radial stiffness provided by New Way. The equivalent stiffness was derived using an end view of the shaft as shown at left in Figure 5 to visualize the deflection of the springs. F_A is the applied force and Δ is the vertical translation of the shaft.

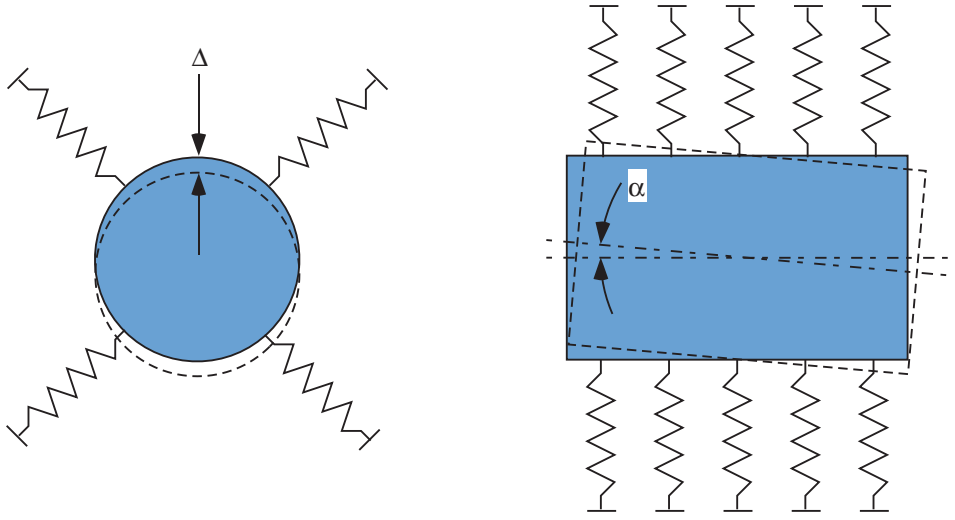

Figure 5. Bed-of-Springs approximation for radial stiffness (end view of shaft at left) and pitch stiffness (side view at right)

Using this model, the equivalent radial stiffness was derived as

$$k_A^r = \frac{2k_{NW}^r}{A_s} \tag{1}$$

The symbol k_A^r is the equivalent radial stiffness that is input into ANSYS and k_{NW}^r is the radial stiffness that is provided by New Way. The variable A_s is the surface area of the shaft inside the bushing. The equivalent radial stiffness is then used in a simulation of the shaft in FEA and the results is a stiffness of 34.1 N/um. FEA simulation with the derived stiffness behaves just like the physical bushing.

Equivalent Pitch Stiffness

As in the derivation of the equivalent radial stiffness, it was known that the equivalent pitch stiffness was going to be a function of the pitch stiffness that New Way provides. Figure 5 also shows a side view of the shaft that was used to derive a model of the equivalent pitch stiffness, which again must be done because the elastic foundation being used in ANSYS is stiffness per unit area. M is the applied moment and α is the pitch angle of the shaft. Using Figure 5, the following expression for the equivalent pitch stiffness is derived

$$k_A^p = \frac{24k_{NW}^p}{L^2 A_s} \tag{2}$$

k_A^p is the equivalent pitch stiffness for ANSYS and k_{NW}^p is the pitch stiffness provided by New Way. A_s is the surface area of the shaft inside the bushing and L is the length of the shaft. The equivalent pitch stiffness is simulated in FEA with a moment applied to the shaft. The rotation observed in the simulation replicates the behavior of the bushing.

A natural frequency simulation was also run in ANSYS using the equivalent stiffness which produced the bushing/shaft couplings first rigid body mode (pitch) at 700 Hz. This is the same value determined in the experiment shown in Figure 4.

2.3 PISTON DESIGN

Three different piston cross sections were evaluated: box, triangle, and cross. ANSYS simulations were run to represent operating forces that the piston would encounter. Each cross section had equal length and mass to have as accurate a comparison as possible. After the simulations were run, each piston received a score based on performance to chose the superior cross section.

Table 1. Results from FEA simulations run on pistons with various cross sections

Scenario	Triangle	Box	Cross
End Load	3	1	2
Pressure	1	2	3
Bending	2	3	1
Rigid Body	2	2	1
Assembly	3	2	1
Total	**11**	**10**	**8**

A score of 3 was given to the cross section that performed the best while the worst received a 1. The end load test represented a vertical end load like the piston would see while machining. Pressure was the ability for a piston to withstand deformation from pressure applied by the bearings. Bending examined the first bending mode of the piston while rigid body was the first rigid body mode of the piston on the bed-of-springs approximation of the air bearing. Assembly refers to degree of difficulty in manufacturing each piston. The triangles ease of assembly is what made it more attractive than the box design.

2.4 PISTON MATERIAL

Choosing a material for the new piston will influence its mass and stiffness. Steel is a very stiff material but has a higher density, and potentially more mass, than competing materials for the application. A stiff, lightweight material is optimal. Aluminum was also considered which is 1/3 the density of steel but also 1/3 of the modulus. Aluminum is a good option, but to get a higher ratio of stiffness to density, composites were examined. After this study, one material that stood out was silicon carbide ceramic. Table 2 shows a comparison between steel, aluminum, and silicon carbide.

Table 2. Properties for piston material

Material	Modulus (Gpa)	Density (kg/m^3)	Modulus/Density, m^2/s^2
Al	70	2700	26
Steel	200	7900	25
SiC	410	3150	130

It is clear that silicon carbide has a superior stiffness to mass ratio (5 times that of aluminum and steel) and that is why this material has been chosen for the FLORA II piston.

2.5 FLORA II DESIGN

The analytical derivation, experimental verification, and FEA simulation that was described earlier in this section all lead to the new FLORA II design shown in Figure 6. The housing dimensions in mm are 90H x 110W x208L. The piston is 70 mm in width across its top and 150 mm long with a moving mass of 250 g. Six porous air bearings provide stiffness for the piston which is driven by a voice coil motor. A linear encoder reads a glass scale attached to the piston for position feedback. As a comparison, the FLORA housing dimensions (mm) are 130H x 205W x 305L with motor and a moving mass of 650 g. The effort described in this Section led into a new design for the FLORA II that will improve optical quality of NRS surfaces while reducing the size and mass of the actuator.

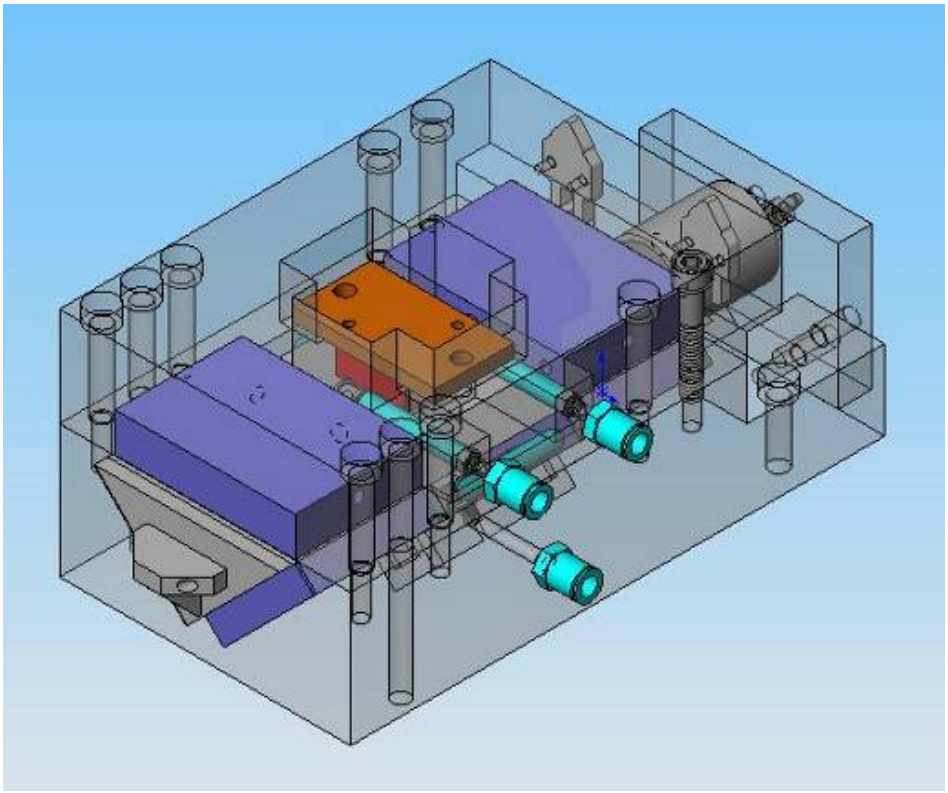

Figure 6. Isometric view of FLORA II with housing and base plate translucent.

REFERENCES

1. Q. Chen, T. Dow, K. Garrard and A. Sohn, 2007. "A Fast Long Range Actuator", Proc. of ASPE, Vol 42, pg 287-290, 2007.
2. New Way Air Bearings. Aston, Pennsylvania, http://www.newwayairbearings.com/

3 ORTHOGONAL CUTTING FOR OBSERVING TOOL FORCE AND WEAR

Brandon Lane
Graduate Student
Thomas Dow
Dean F. Duncan Distinguished Professor
Department of Mechanical and Aerospace Engineering
Ronald Scattergood
Professor, Department of Materials Science and Engineering

3.1 INTRODUCTION

The research objective of this new NSF award is to test the hypothesis that micrometer-amplitude vibration of a diamond cutting tool will reduce forces, improve surface finish and decrease wear of the tool. Faculty members and graduate students in material science and mechanical engineering will measure and model the material removal process and define the parameters that control tool forces, tool wear and surface finish for the selected materials. Materials have been chosen to provide a range of physical and chemical properties that will test proposed concepts of material flow, temperature generation and wear mechanisms. Unique techniques for measuring the chip geometry, surface finish, tool edge sharpness and diffusion of the carbon from the tool to the chip/workpiece will be used to describe the details of the process. This project will quantify the vibration conditions needed to create high-quality surfaces on materials such as steel, glass or ceramics that were thought to rapidly wear diamond tools. Steel is the most frequently used engineering material due to its excellent properties, availability and low cost. A national and global demand for ultra-precision steel parts and systems with sub-micrometer accuracy exists in automotive, medical and optical industries. Precision glass and ceramic components are also in high demand.

Vibration assisted machining (VAM) has been incorporated in precision machining processes since the early 90s, and has proven benefits when compared to standard DT such as reduced tool forces and tool wear. During the VAM process, the tool is lifted from the workpiece and returned to cutting in cyclic manner at high frequencies (1000s of Hz). This motion leads to improvements in tool wear and forces, yet maintains high quality surface finishes. Due to the advantages of VAM, materials that were previously deemed unfit for machining because of their high abrasiveness, brittleness, or high ferrous content, can be machined to optical quality finish.

While these benefits are remarked upon in numerous scientific articles, results are empirical, and no one has addressed the scientific principles behind VAM, nor quantified these improvements with regard to changing process parameters. This project will study this machining process in detail, quantify improvements in surface finish and tool wear, and elucidate the reasons why such improvements are possible.

During the initial phase of the project, a number of tasks must be accomplished before experiments with VAM can begin. Data regarding tool wear, tool forces, and surface finish must be obtained for the standard DT process as a baseline for study and comparison of VAM results. Experimentation practices must also be perfected and metrology procedures must be developed.

3.2 TOOL FORCE MEASUREMENTS

3.2.1 EXPERIMENTAL SETUP

The orthogonal cutting experiments highlighted in this Section are a means of finding force and wear data for standard DT practice. Al 6061-T6 disks were cut using a large nose radius diamond. The hard particles in the 6061 alloy will create substantial and measureable abrasive wear on the diamond tool based on previous experimental work [1]. The disk width was selected to be less than half that of the diamond, so that a centered area of wear on the tool could be observed and compared against areas untouched by the cutting material. This relatively simple setup allowed the students to gain an introduction to diamond truning, data acquisition, and metrology. It also provided a first look at the wear patterns and tool forces that can be later compared with those obtained through similar VAM experiments. Although force measurements from this experiment are somewhat inconclusive, wear patterns observed on the diamond tool are of interest.

A fixture was built to hold aluminum cutting disks turned in the DTM. The fixture includes a 3" cylindrical base and cover plate. The cutting disk is placed between the cover plate and base and is fastened using ¼" cap screws. Both base and cover plate are made from Al 6061. Surfaces on the two fixture parts were sanded to ensure flatness, and to minimize distortion and excessive runout of the cutting disk. The cutting disks were cut from 0.032" thick Al 6061 with diameters of 130mm. This allows 1.11" of disk to protrude from the fixture base. This protrusion length allows for approximately 2.1 Km of cutting per disk at a depth of cut of 2.5μm while maintaining a relatively high stiffness of the supported cutting disk. Table 1 summarizes cutting parameters used for each individual disk.

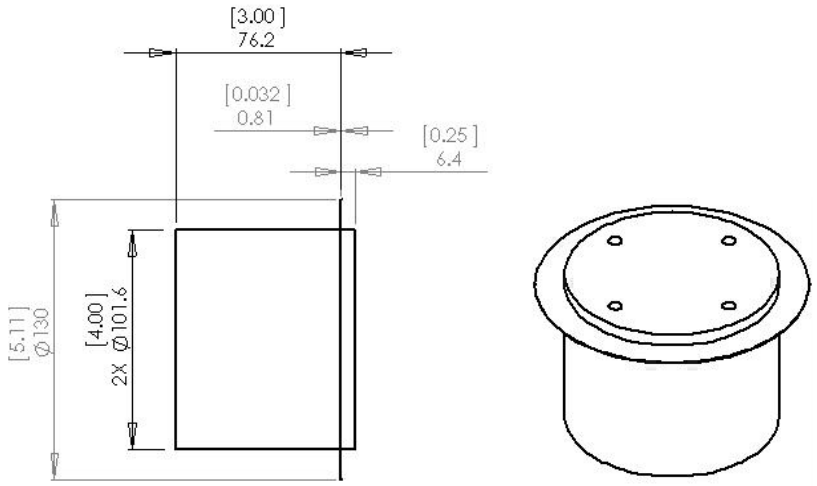

Figure 1. Side and isotropic views of test piece fixture and cutting disk assembly. Dimensions are in mm [in].

Table 1. Cutting parameters for each aluminum cutting disk.

Spindle Speed	500 rpm
Depth of Cut	2.5 μm
Tool infeed rate	1.25 mm/min
Total Cut Length	2.105 Km
Reduction in Disk Radius	14.5 mm
Continuous Cutting Time	11.6 min
Diamond Nose Radius	5.454 mm

To measure cutting forces, a three axis piezoelectric load cell (Kistler 9251A) was incorporated into the tool holder. Figure 2 shows the setup used for this experiment. Once the load cell was preloaded in the holder to the prescribed load, it was connected to a three channel charge amplifier and digital oscilloscope. The charge amplifier converted load cell charge into an amplified voltage signal that could be measured by the oscilloscope. To calibrate the load cell setup, known masses were hung from the diamond tool holder with a light wire in the x and y directions that coincided with cutting force (*Ft*) and thrust force (*Ft*) directions. Calibration transfer functions were then found for *Ft* and *Ft* given voltage changes read by the oscilloscope. The oscilloscope was also capable of saving force data, and therefore was used for data acquisition.

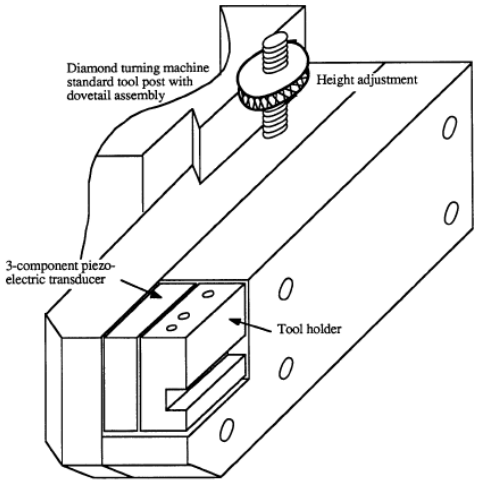

Figure 2. Tool post, load cell, and tool holder setup [1]. The load cell is located between the tool holder and block and preloaded via M6 bolt.

A G-code program was written for the ASG2500 DTM that would cause the diamond to cut the disk for 0.5 Km, retract from the workpiece and fee in again. While the diamond is retracted, the oscilloscope is triggered to start data acquisition. This allows the piezoelectric load cell to be zeroed between measurements to avoid any problem with drift of the reading. A 5.454 mm radius, 2 mm wide diamond tool was mounted in the tool holder. The fixture was set and centered on the DTM vacuum chuck, and a steady oil stream was directed at the diamond tool. Three disks were cut in this manner, resulting in 12 total force data sets, and a total cutting distance of 6 Km.

3.2.2 EXPERIMENTAL RESULTS

Force Data

There was a problem with the force data collected for the first disk (0-1.5Km cutting distance). The diamond tool was not tight in the tool holder. Once the problem was recognized and corrected, force measurements were able to be obtained from data sets from 2.0 – 3.5 Km. Unfortunately a second set of problems occurred – a mistimed oscilloscope triggering or out of range data. Figure 3 shows data collected at 4.0 Km of cutting that is typical of that collected for 4.5, 5.0, and 5.5 Km.

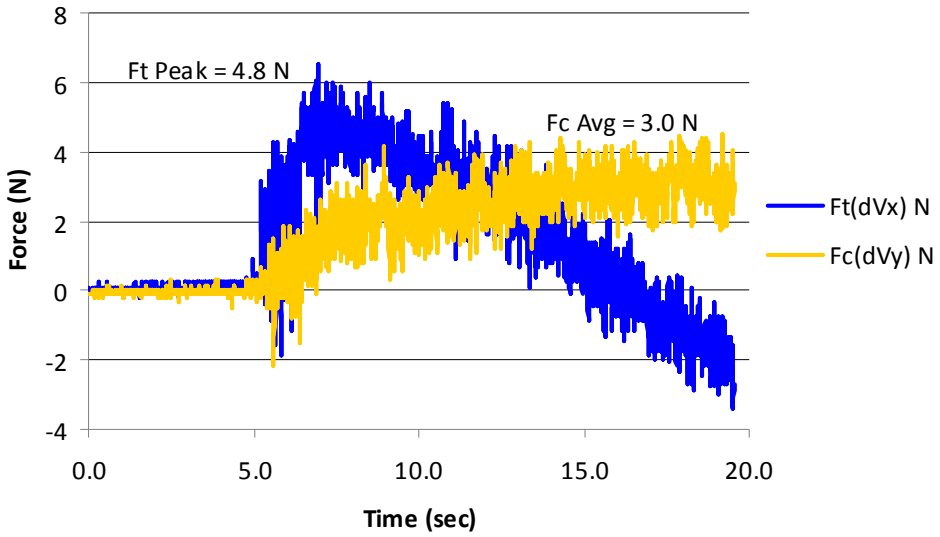

Figure 3. Force data collected on the third disk at 4.0 Km of total cutting distance.

Once the tool contacted the cutting material, the thrust force increased to a point, then decreased linearly, signifying that the material was 'pulling' the tool with an increasing magnitude. This is intuitively wrong, and previous similar experiments [1] did not note such behavior. Despite the erratic behavior, force magnitudes could be estimated by observing the relative increase from a no-load condition, such as those shown in Figure 3, and given in Table 2. These forces were larger than expected , with expected *Ft* magnitudes of around 1.5 N based on material hardness, and *Ft* magnitudes larger than those of *Ft*, as observed by Drescher in [1].

Table 2. Summary of force data from last four data sets.

Cut Distance (Km)	*Ft* Peak (N)	*Ft* Average (N)
4.0	4.8	3.0
4.5	5.3	2.8
5.0	5.9	3.6
5.5	6.0	4.5

Tool Wear Geometry

Multiple images of the diamond rake face were taken with a Zygo NewView white light interferometer before and after cutting 6 Km. A wear trench was found to have formed in the general vicinity on the tool where the aluminum disks were cut. The deepest part of this trench was located approximately 6 μm in from the cutting edge and ran approximately 1 mm parallel.

Boundaries of the trench and center of the tool were found by locating the tool edge at the center of the NewView monitor display, noting the stage position, then locating a point of interest and noting the difference in state positions. The left image in Figure 4 shows a schematic of the location of this wear trench with respect to tool edges.

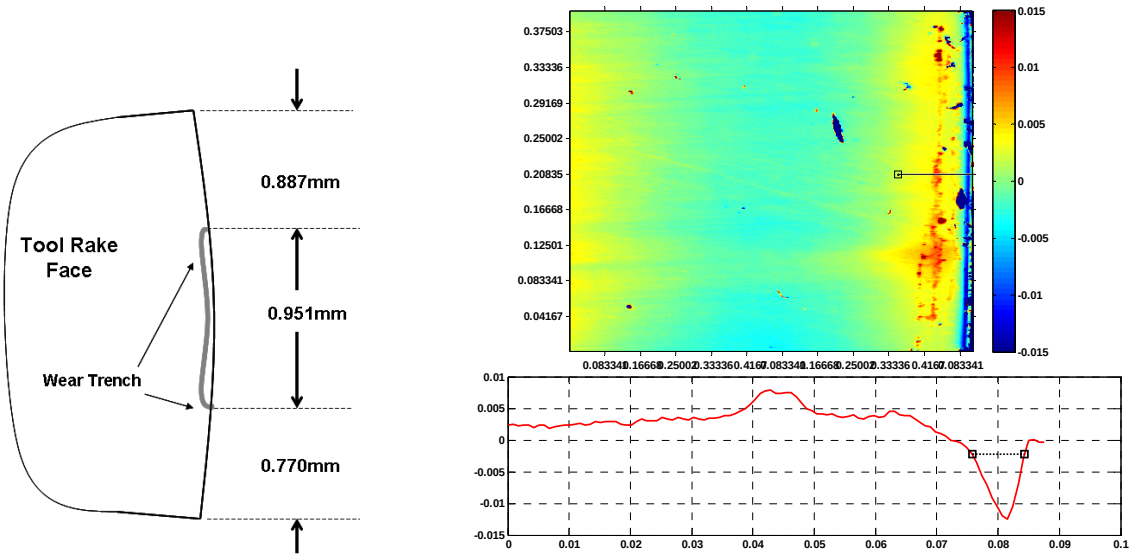

Figure 4. Schematic of tool rake face and relative vertical location of wear trench (left) and Matlab Slicer program view of rake face NewView data obtained at 10x1.3 zoom and 640x480 pixels (right). Vertical scale is µm and horizontal is mm.

The upper plot at the right in Figure 4 shows the NewView interferometer rake face surface data obtained with the tool edge and wear trench on the right. X-Y axes in upper plot are in µm, while the color bar Z axis is in nm. The lower cross section plot shows the X-Z data obtained from the section indicated by the horizontal stripe in the upper image that is at the approximate center of the tool edge. The wear trench is visible on the right hand side of Figure 4 and is shown at further enlarged view in Figure 5.

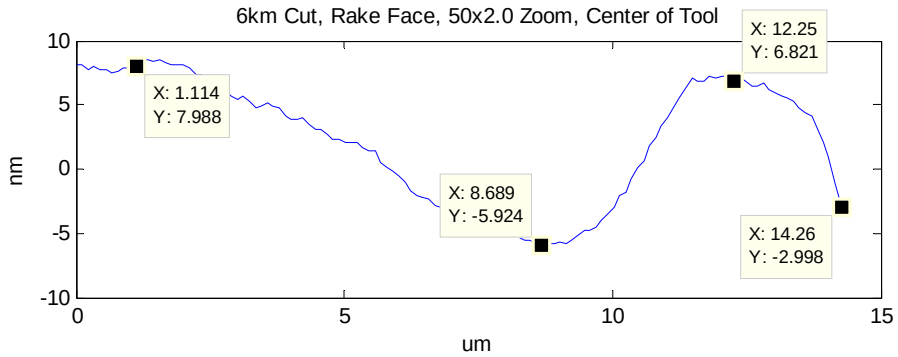

Figure 5. Slicer cross section plot of tool cutting edge showing location of points of interest on the wear trench. These points show a trench depth of approximately 12.75nm.

Figure 6 shows the wear profile close to the top edge of the tool in Figure 4. Note that the wear trench comes out of the tool at the width of the aluminum sheet. The depth of the trench is small, about 15 nm, and occurs over 10 µm near the edge. The damage to the tool at the edge of the aluminum sheet is probably caused by damage from abrasive used to sand the face of the disk, a practice that will not be repeated.

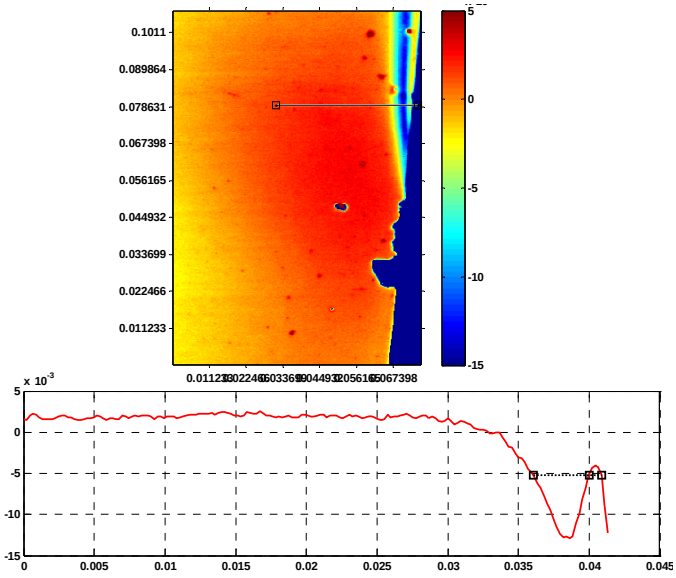

Figure 6. Matlab Slicer program view of rake face approximately 0.887mm from the tool top edge (Figure 4) showing the wear trench exiting towards the tool cutting edge. Upper image is inverted vertically from actual tool position. Vertical scale is µm and horizontal is mm.

3.3 CONCLUSIONS

Force Data

Both signals for *Ft* and *Ft* were noisy, with variations nearly 75% the average values for *Ft*. It was hypothesized that there might be vibration induced at the frequency of the spindle rotation (8.3 Hz). Spectral analysis was conducted via Microsoft Excel for the voltage data obtained from the oscilloscope, but no substantial frequency peaks were found. The sampling frequency of the oscilloscope depends on the horizontal time/division setting, with a 100 Hz sampling frequency occurring at 1 sec/div. Based on Nyquist criterion, spectral analysis is only possible for frequencies below 50 Hz and higher frequencies may be aliased to lower frequencies.

Future experiments will include exchanging the load cell and calibrating it in-situ. This will entail loading the tool holder with calibration masses so that the induced load acts in the same

direction as the expected cutting and thrust forces. This will be done while the tool holder and tool post is secured on the DTM stage using a data acquisition rather than oscilloscope.

Interferometer Data

Surface roughness data was readily available via the Zygo NewView white light interferometer. Imaging of the flank face of the tool, however, was difficult due to the curvature of the face. Reduction in the edge radius of the tool from wear was immeasurable with the interferometer, but methods have been proposed [1] to measure the edge radius using a scanning electron microscope (SEM). Small strips of platinum will be deposited over the tool edge at various locations. This will add contrast to the edge and facilitate the tool edge radius measurement in the SEM. It will also provide reference for future interferometer and SEM measurements. It was also observed in the white light interferometer that there had been a small amount of aluminum pickup on the rake face of the diamond tool. This may have increased measured tool forces from those that would be observed from a clean tool.

REFERENCES

1. Drescher, J.D., Tool Force, Tool Edge, and Surface Finish Relationships in Diamond Turning. PhD Dissertation, North Carolina Sate University; 1991

4 KINOFORM LENS FABRICATION

Alex Sohn
Precision Engineering Center Staff

4.1 INTRODUCTION

In the course of a project to develop Fresnel lenses for scanning systems, the diffraction due to the discontinuities inherent in a Fresnel lens lead was investigated. This diffraction can have undesirable results by redirecting light away from the focused spot and into other spots. Diffraction does not, however, have to be detrimental. The concept of a Kinoform lens [1] is to tailor the diffraction to enhance the focusing ability of the lens instead of disturb it. With grooves spaced at precise intervals, it is theoretically possible to achieve a spot size as good as, or better than, without diffraction. In the real world, however, manufacturing such lenses requires some compromises and challenges to available fabrication capabilities.

4.2 MACHINING

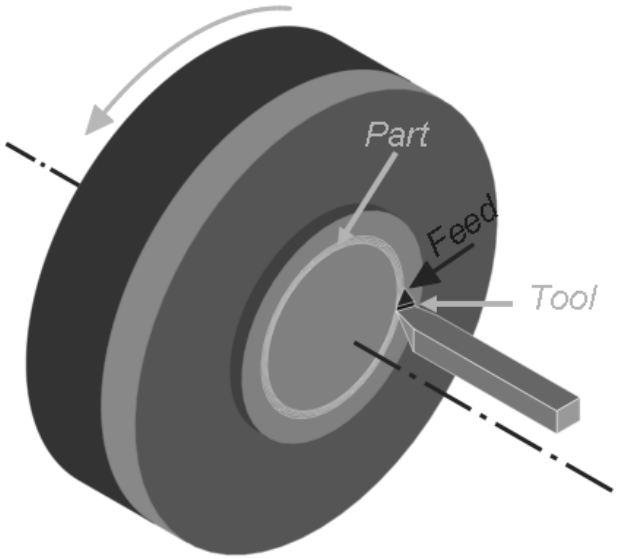

Figure 1. Setup for preliminary groove cutting tests.

The spacing and angle of the facets on the Kinoform lens determine the location of the refractive and diffractive beams. For a phase match order of M = 1 [2], the groove spacing must be very small at larger apertures and the lens becomes difficult to fabricate; for example, a 200 mm f/l.

lens at r = 11.5 mm has a 6 μm spacing between grooves. Even when the phase match order is increased to M = 5, the groove spacing is still very small. As a result of these small features, the lens cannot be contoured with a round-nosed tool but rather must be machined as a series of plunge cuts with a sharp tool. The side of the dead sharp tool forms the flat refractive portion of the lens and must be rotated at each plunge to change the angle as the groove radius is changed.

4.2.1 PRELIMINARY GROOVE CUTTING TESTS

Since kinoform lens grooves with the 5-50 μm spacing required have not been fabricated at the PEC by turning, several test cuts were made in PMMA (PolyMethylMethAcrylate) to determine the best cutting conditions and procedures before cutting an actual lens. Of primary interest was whether there was any appreciable influence of the cutting direction on the final parts. Figure 1 shows the diamond turning setup where an annular ring of grooves is cut with the dead sharp tool tilted at an angle.

The grooves were cut with the tool at a fixed angle in a rigid stationary. To test the impact of cutting direction, plunge cuts were preformed both from the inside to the outside of the part and vice versa as shown in Figure 2. This change in cutting direction produces a significantly different chip, as shown if Figure 2, though the overall amount of material removed in the same. The SEM micrographs in Figure 3 show a distinct difference between the surfaces as a result of the two different cutting directions. It appears that while the outside-to-inside cut produced grooves that are relatively free of burring, the inside-to-outside cuts produced large “curtain” like burrs that were firmly attached to the tips of the grooves. This is believed to be caused by the chip remaining attached at the tip of the groove because the tip of the previously cut groove is now unsupported at the left hand end and can easily deform above the cutting edge of the tool.

Based on these results, all subsequent cuts were made in the outside-to-inside direction. An additional set of tests was performed using different coolants. These tests showed little difference between the use of ionized air, mineral spirits or cutting oil. Given that the coolant did not matter, ionized air was used for all tests since lenses cut in this way are much easier to clean.

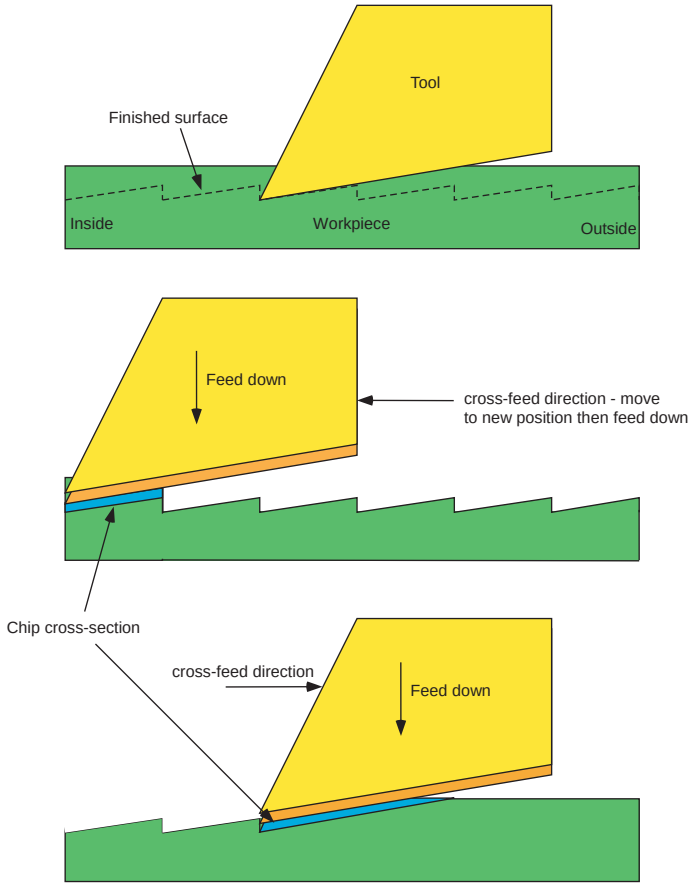

Figure 2. Preliminary cutting tests showing the cutting process (top) and the different cutting directions, outside-to-inside (middle) and inside-to-outside (bottom).

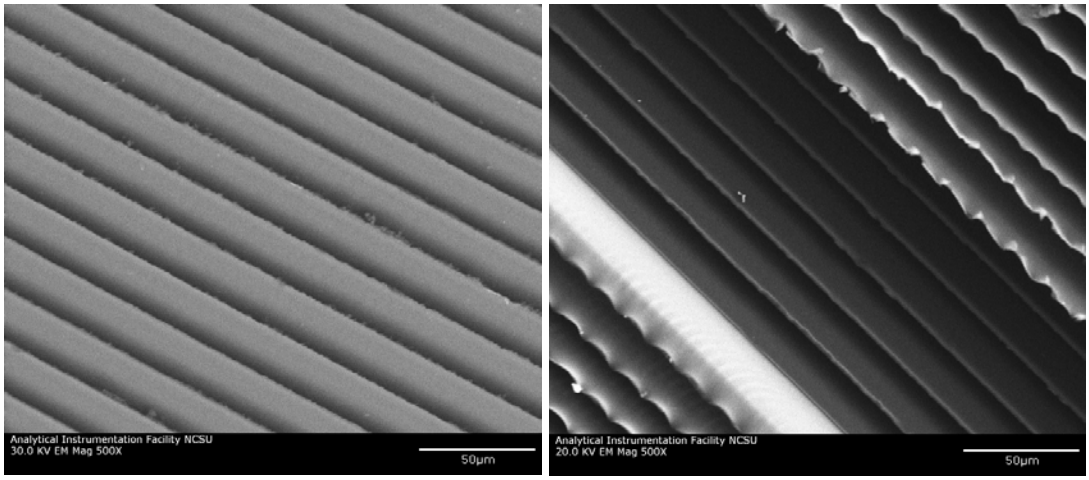

a) b)

Figure 3. The chip cross section differs significantly for a) outside-to-inside and b) inside-to-outside cutting.

4.2.2 FLEXURE-BASED TOOL HOLDER

Ideally, a rotary axis (oriented perpendicular to the X-and Z- axes of the diamond turning machine) would be used to rotate the tool. Unfortunately, neither of the diamond turning machines at the PEC has such a rotary axes, so a temporary solution was devised to machine small segments of Kinoform lenses. This tool rotation device was based on a flexure mechanism shown in Figure 4. The flexure is mounted on the X-axis of the DTM and a linear stepper motor axis is used to push on the actuation point to rotate (and translate) the tool.

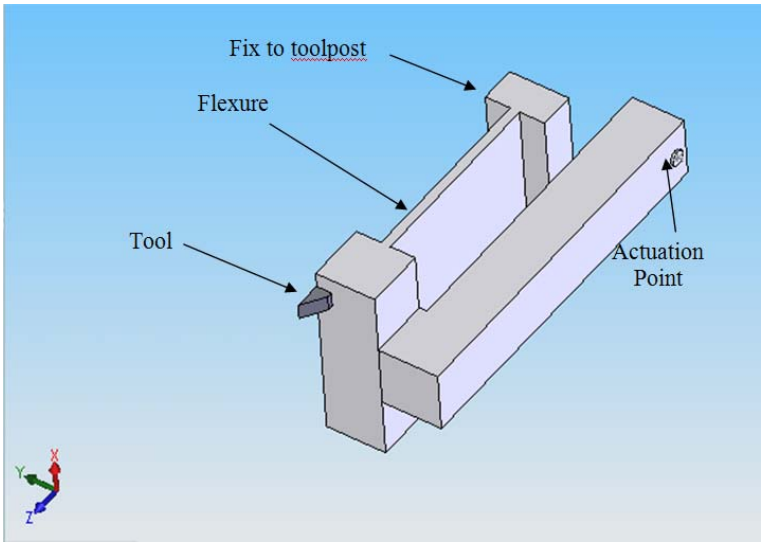

Figure 4. Flexure based tool rotation mechanism. A flexure that is very stiff in the vertical direction allows the tool to rotate in the Y-Z plane.

The force at the actuation point produces a force and a moment at the tool. The moment rotates the tool and the force moves it in the y-direction creating a small motion in the z-direction (depth of cut). The flexure was designed to allow actuation at reasonable forces without exceeding the yield strength of the aluminum flexure. A finite element model was used to evaluate the stress vs. deflection for different flexure designs. The results indicated that the flexure could tilt the tool up to 2 degrees while staying within 20 % the yield stress of 6061-T6 aluminum.

The flexure bends predictably and causes deflections of the tool that can be modeled. Parameters of interest are 1) position at the actuation point, 2) deflection angle, and 3) position of the tool tip. After modeling, the same parameters were measured on the mechanism and a linear relationship (close to the calculated one) between the tool position and angle was developed.

However, the range of tilt angles needed for the kinoform lens with a 200 mm focal length and a 100 mm aperture requires a 14° range of angles from center to outside diameter. This range

would not be possible with a flexure based tool holder a more flexible solution involving a ball-bearing goniometer was implemented.

4.2.3 TOOL HOLDER USING BALL-BEARING GONIOMETER

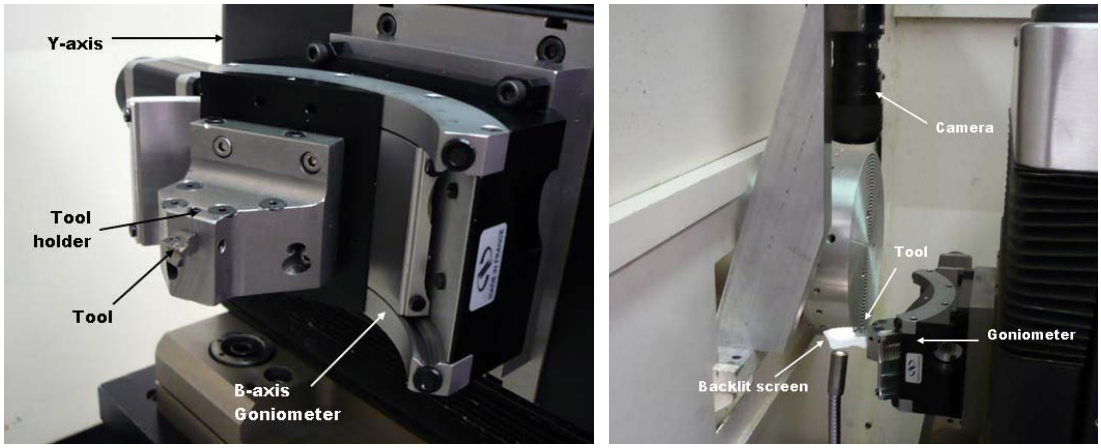

(a) (b)

Figure 5. Newport Goniometer mounted on y-axis of diamond turning machine with a) showing a closeup of the axis and b) showing the placement on the DTM with camera looking down.

Mounting and Control of the B-axis

Equipment funding from NC State University ($5K) became available in the spring of 2008 and a ball-bearing goniometer B-axis was purchased to fabricate a larger range of angles than is possible with the flexure design. The B-axis is mounted to the Nanoform 600's Y-axis and the tool is held securely via a non-adjustable toolholder as shown in Figure 6. The control integration of the goniometer axis is performed using an external D-space DSP controller. The D-space system reads axis data from the Nanoform 600's Zygo ZMI 501 laser system quadrature output. This axis position data is then used to find a corresponding B-axis coordinate position in a lookup table generated off-line. The B-axis coordinate is then converted to step and direction signals and sent to the stepper driver via the D-space's digital I/O interface. The digital I/O also interfaces to the B-axis' limit and home position flags. This allows the axis to be homed at the zero (centroid) position and provides an absolute reference.

TOOL CENTERING

Centering the tip of the dead-sharp tool on the axis of the goniometer stage (B-axis) is performed by correcting the motions of the X and Z-axes of the DTM instead of actually repositioning the

tool. To calculate the necessary motions of the X and Z-axes, the tool offset must first be measured. To measure tool position, a CCD camera with 100X magnification optics and crosshair reticule are mounted above the tool as shown on the right in Figure 5.

Figure 6. Image from video camera used to find the errors in tool edge positioning as a function of the angle of rotation of the ball-bearing goniometer

With the tool in focus, the machine axes are moved to make the tip of the tool coincident with the crosshairs. A monitor shows the tool relative to the crosshairs in Figure 6.

The procedure for B-axis centering of the tool is as follows:

1. Zero the X and Z axes at B=0. Measure X and Z-positions as a function of B. A minimum of three positions is required. More points will yield a more robust fit that sees less influence from individual measurement errors, particularly since the maximum included angle of points is 90º.

B	X	Z
B_1	X_1	Z_1
B_2	X_2	Z_2
.	.	.
B_n	X_n	Z_n

2. Fit X, Z data to obtain R, X_c and Z_c. Use **circfit** function in Matlab and also find initial angle, B_0, which is the angular offset to the center of the circle.

$$B_0 = \arctan\left(\frac{Z_c}{X_c}\right) \tag{14}$$

3. Now, any point's corrected X and Z position can be calculated from the B-axis position:

$$\begin{aligned} X' &= X_c + R\sin(B - B_0) \\ Z' &= Z_c + R\cos(B - B_0) \end{aligned} \tag{15}$$

where the addition of the circle center coordinates offsets the tool to allow offsets to be relative to *B=0*, which can then be used to touch off on the part.

4. The corrected positions X' and Z' can then be added to the programmed positions as a function of B in any part program.

4.2.4 CONTROL

The coordinates and angles of the grooves are calculated using the diffraction modeling software developed by Garrard (2007 Annual Report). The form of these coordinates is X and Z at the bottom of each groove and a slope for each facet. These points are read into Excel, where a spreadsheet adds the X and Z axis corrections and appends the G-code components to allow the PMAC-NC controller to run the part program. Also added are the remainder of the points required to make the series of plunge cuts and a dwell command for at least one spindle rotation at the bottom of each groove. The spreadsheet is saved as plain text to avoid conflicts with the controller which often result from Unicode text (default excel text format). The coordinates and angles are also processed into a set of corrected X and angle (B-axis) values that are saved as a plain text lookup table for the D-space program. The D-space controller is programmed in Simulink and has a Control Desk user interface.

4.3 METROLOGY

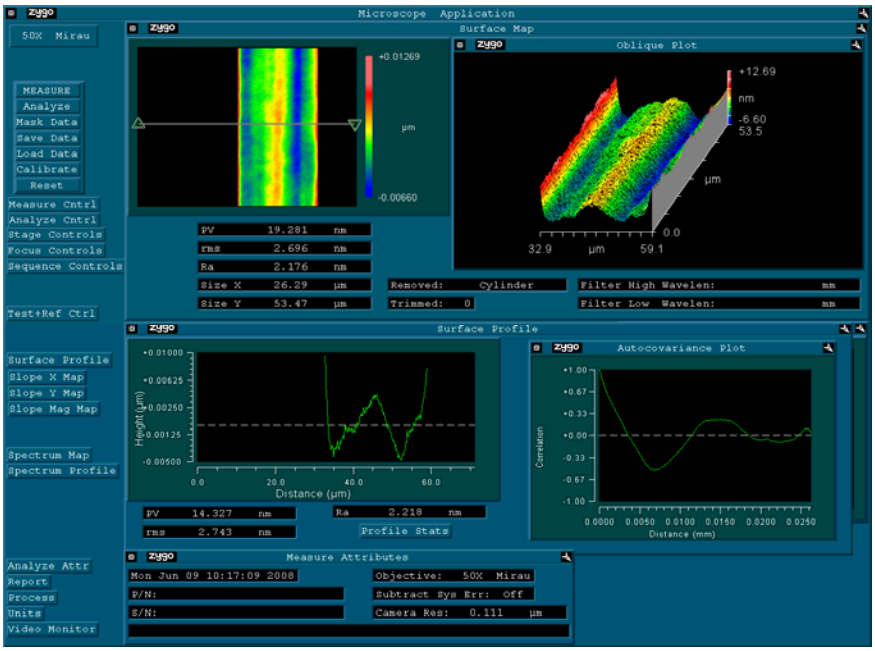

Figure 7. Surface finish of a facet of the kinoform focusing lens. The face of the facet is flat to 19 nm over a width of 28 µm and the surface finish is 2.7 nm RMS.

The surface finish and flatness of the kinoform lens facets is excellent. Figure 7 shows the surface finish of one facet of the lens. It is about 28 µm wide and is flat to 19 nm over this width; that is, about one part in a thousand. The surface finish is also exceptional - 2.7 nm RMS. Some of the facets had high frequency features from the plastic shearing during machining, but in general, the surface illustrated in Figure 7 reflects the quality of the machined features.

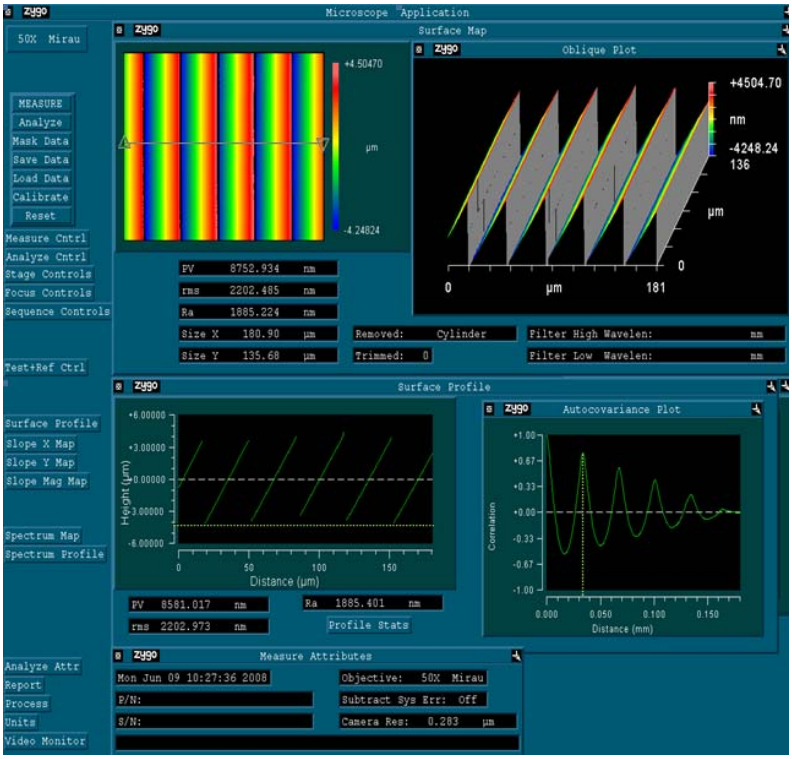

Figure 8. Shape of selected kinoform facets machined on the DTM. Note the variation in the height of the grooves (approximately 1 µm) in the lower left-hand section of this figure.

Figure 8 shows a white-light interferometer (Zygo NewView) image of a number of grooves over a surface area which 180 µm long and 136 µm wide. The depth of the grooves in this section of the lens is approximately 9 µm deep with a spacing of 33 µm (see marker on lower right autocovariance plot) for a tilt angle near 14 degrees. One feature of the grooves which is a concern is the variation of the depth of adjacent facets as illustrated in the lower left cross section of Figure 8. While this single cross section does not definitively identify a problem, it indicates that variations in the depth of cut caused by goniometer repeatability or non-synchronous spindle errors may be a factor in the performance of the lens.

The kinoform lens in was designed to have the path length from adjacent facets to the focus to increment exactly 7 times the wavelength or 5.55 µm. This factor (called the phase match order M in the derivation earlier in this report) matches the phase of the refracted light so that the

location of the constructive interference can be controlled. However, to achieve this design, the tolerance on the facet tilt and location must be carefully controlled. The variation illustrated in Figure 8 may be an indication of a fabrication problem.

4.4 CONCLUSIONS

While the machining process for the kinoform lens still requires some refinement, the results of the first part are encouraging. To achieve higher tolerances on groove test, believed to be a major factor in somewhat lackluster optical performance of the lens, it is likely that a more accurate tool tilting mechanism will have to be employed. Apart from this, the surface quality results of the lens were excellent, showing that the plunging process is feasible for generating the stepped conical features of a Kinoform lens.

REFERENCES

1. Buralli, DA, G. Michael Morris, GM, and John R. Rogers, JR, “Optical performance of holographic kinoforms”, APPLIED OPTICS, Vol. 28, No. 5, March 1989, pg 976-983.
2. K.P. Garrard, *Fresnel Design Software*, 2007 PEC Annual Report, pp1-23.

5 PERFORMANCE OF FRESNEL OPTICS

Thomas A. Dow
Dean F. Duncan Distinguished Professor
Department of Mechanical and Aerospace Engineering
Kenneth Garrard and Alex Sohn
Precision Engineering Center Staff

5.1 INTRODUCTION

Fresnel lenses are a type of lens that eliminates the bulk of a conventional lens by collapsing the lens thickness while retaining surface slopes necessary for focusing. Figure 1 shows the Fresnel lens equivalent of a conventional lens. For a rotationally symmetric lens, the discontinuities or grooves formed when collapsing the lens are annular. This produces a much thinner lens, particularly for large apertures.

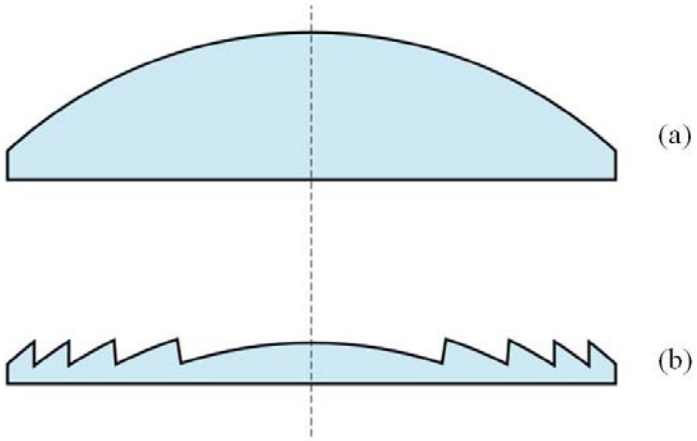

Figure 1. A Fresnel lens (b) is basically a collapsed version of a conventional lens (a).

The advantages of a Fresnel lens are that more light is transmitted due to less absorption and dispersion in the material and with more uniform thickness, a Fresnel lens is typically easier to replicate by molding. The latter of these two reasons is why Fresnel lenses are being considered for improving scanning systems in this project. Cost is a driving factor in scanning systems for laser printers, so a switch to an easily moldable Fresnel lens could provide a significant advantage. Fresnel lenses are intended as purely refractive lenses. A common misnomer is to refer to a diffractive lens as a Fresnel lens. Properly, this is called a Fresnel zone plate. Separate and distinct from a Fresnel lens, a zone plate focuses light using diffraction from a series of annular rings. A Kinoform lens combines refractive and diffractive properties of Fresnel lenses

and zone plates to produce a more efficient diffractive lens that can also cancel chromatic aberration.

Fresnel lenses have found their way into a number of applications including infrared motion detectors, overhead projectors, solar collectors, theatrical lighting and many more. Typically, Fresnel lenses are used for non-imaging applications where the effects of scatter and multiple internal reflections are not critical problems. While it also qualifies as non-imaging, the application of focusing a rapidly scanning beam to a small spot size is, however, challenging.

5.2 DIGITAL CAMERA

The technique for measuring spot sizes has evolved with the project. The initial sensor was a Canon EOS Rebel XT SLR with an 8 Mpixel color array but this proved unsatisfactory due to the method the camera uses to process the intensity and color of the incoming light. A monochrome Cohu 7700 camera was borrowed but it did not have the sensitivity needed for the measurements. Finally a monochrome Epix 5M10 camera (shown at right) with the proper sensitivity and resolution was purchased. This camera is much easier to use than the Canon camera because it has video capability so the exposure can be set and intensity viewed prior to saving the spot measurement.

This camera has 2592 x 1944 array of photocells spaced 2.2µm apart. The overall size of the array is 5.7 mm wide by 4.28 mm high. It has a sensitivity of 1.4 V/lux-sec at 550 nm illumination. The camera uses a pair of A/D converters to send the data from each sensor to the video board in a PC. One row uses the first A/D and the next row uses the other converter. Unfortunately, each of these converters has a slightly different gain and as a result adjacent pixels have an offset value. After much discussion with the manufacturer, it was decided to average adjacent pixels and the resulting horizontal and vertical resolution is 4.4µm.

A collimated laser source was provided by Lexmark for the experiments. This solid state laser has a wavelength of 650 nm and a 4 mm beam diameter.

5.3 DIFFRACTION FROM A NARROW SLIT

A pair of razor blades were glued to an aluminum block with a spacing on the order of 100 µm to test the spot size measurement. The laser light illuminated the slit and the resulting diffraction pattern can be measured with the camera in both spacing and intensity. This pattern can then be compared to that expected for the light wavelength, the slit gap and the slit to camera spacing.

The camera setup is shown in Figure 2. The Epix camera has a RJ45 cable to connect it to the video board on the computer. It has no lens. The camera is mounted on a xyz stage and the laser is attached to an optical rail along with the slit. The right side of Figure 2 shows the 88 µm width of the slit as measured in a light microscope.

The diffracted intensity pattern in Figure 3 was calculated using Fraunhofer's approximation where the diffracted energy can be written as:

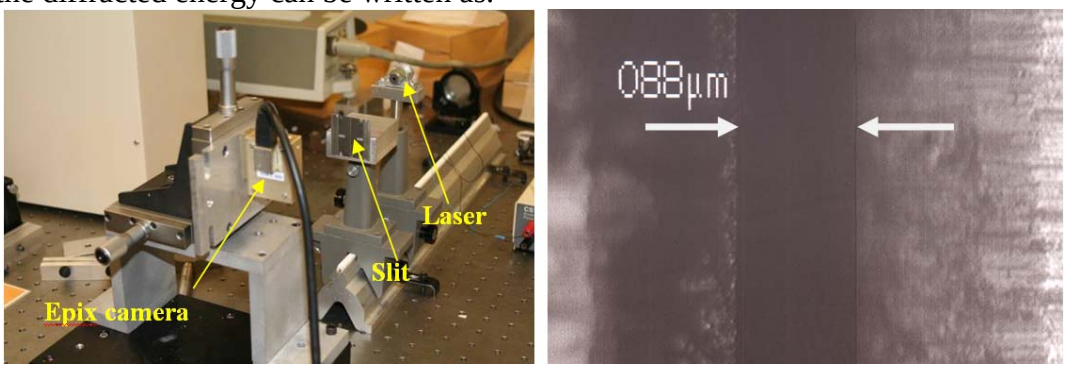

Figure 2. Camera setup to measure the diffraction from a slit and the slit gap measurement

$$I(x) = \frac{\sin^2[\pi(d/\lambda)\tan(x/y)]}{[\pi(d/\lambda)\tan(x/y)]^2} \tag{1}$$

where d is the slit width, λ is the wavelength of light, x is the distance on screen, and y is the distance from the slit to the camera which in this case was 93 mm. The comparison of the amplitude and location of the diffraction peaks provides great confidence in the camera system for measuring the features of interest.

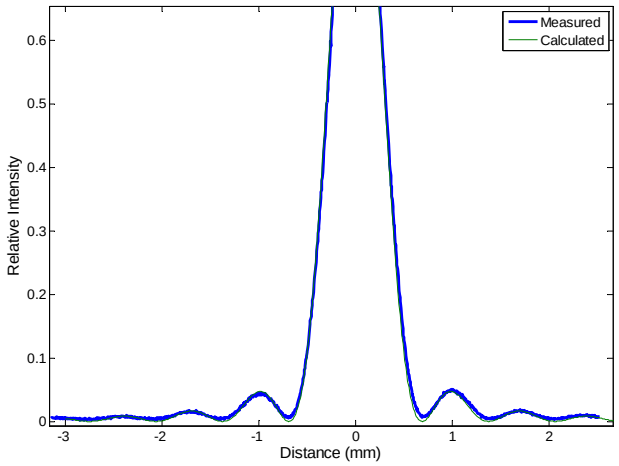

Figure 3. Comparison of the relative intensity vs. horizontal position for the laser beam through an 88 µm slit placed 93 mm from the camera array.

5.4 200MM FOCAL LENGTH GLASS LENS

The objective of this project is to develop Fresnel focusing and scanning lenses. Before beginning the lenses tests, experiments were conducted using a commercial glass lens to measure the quality of the spot. This would be the best case for the Fresnel lens measurements that follow. The collimation lens on the laser was adjusted to keep the beam size constant as the laser is moved away from the camera. After adjustment, the beam diameter changed only 30 µm for a 10cm change in beam to camera distance.

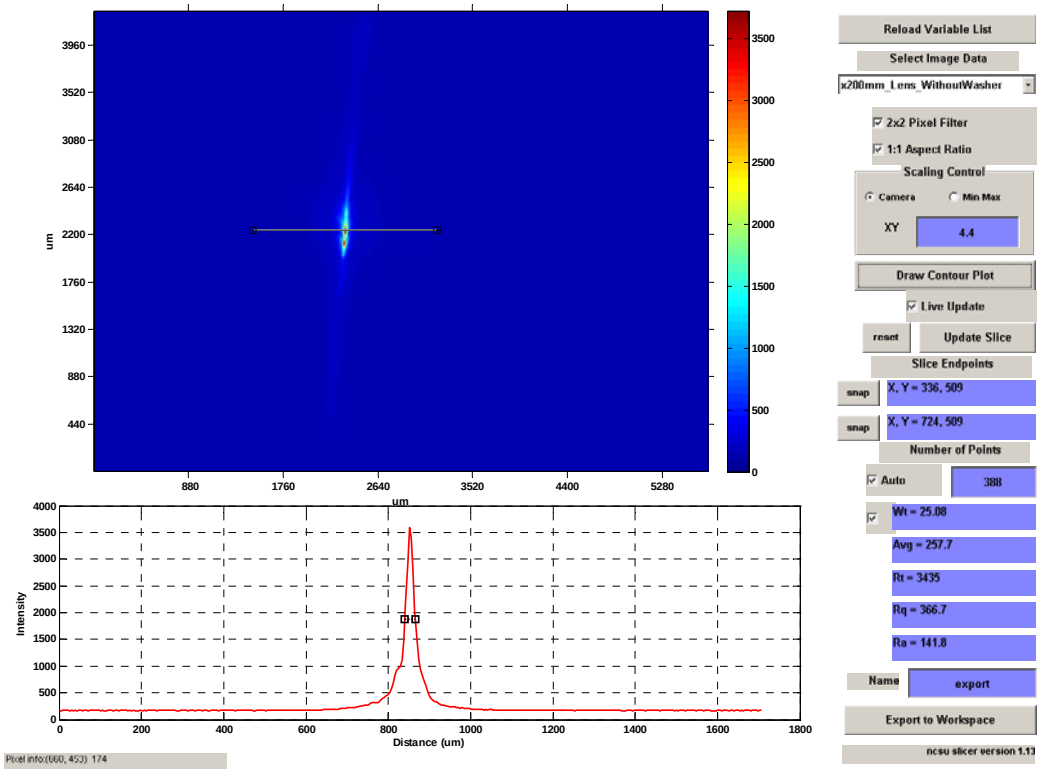

Figure 4. 200mm Glass Lens (FWHM=25.08µm)

The spot size of the glass lens is shown in Figure 4. Clearly it is not a circular spot and the reason is not clear. The lack of symmetry is not due to the lens because rotating it kept the spot size as shown. One possibility may be a lack of collimation in the incoming beam. The spot is characterized as two peaks with wings that move away from these peaks. The spot size in the lower part of this figure is measured through one of the peaks and perpendicular to the line between peaks; that is, through the black line in the image. The spot size (Full Width Half Maximum) is 25 µm.

5.5 CONICAL FRESNEL LENS

The next optical surface measured was a commercial conical Fresnel lens obtained from Edmond Optics. The lens is 264 mm in diameter with a 203 mm focal length. It has uniform groove spacing of 127 µm or 200 grooves per inch.

Surface Features of Fresnel Lens The surface profile of the commercial conical Fresnel lens was measured using the Zygo NewView white light interferometer. The image taken near the center of the aperture (left image in Figure 5) shows the overall shape but also indicates a number of imperfections across the surface. The features near the center have a height of about 1.7 µm. At the right in Figure 5, the features near the outer edge of the lens are shown. Here the amplitude of the features is about 3 µm but the imperfections seem smaller at this increased vertical range.

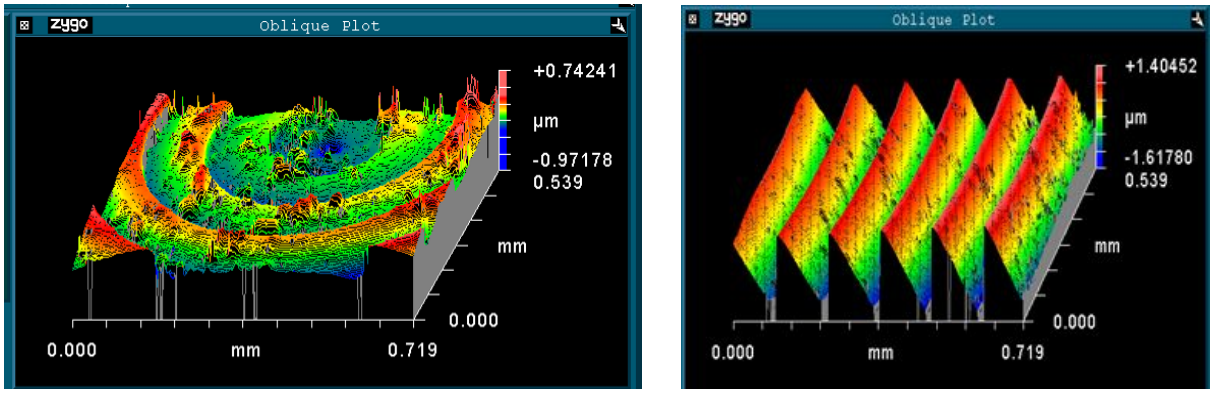

Figure 5. Optical profilometer measurement of center (left) and outside edge of a commercial conical-groove Fresnel lens. Note the poor surface quality near the center.

Spot Size Measurements The camera is centered on the laser beam (Figure 6) and the lens is placed between the camera and laser at a distance from the camera near the 200 mm focal length. The grooves are facing the camera so the light is incident on the flat back of the plastic and refracts/diffracts off the faceted front surface. The lens moves with the camera but the laser is stationary so the effect of illuminating the lens away from the center can be measured.

A spot was measured at intervals on- and off-axis as shown in Figure 6. The exposure was kept constant throughout the measurements. Figure 6 shows the shape of each spot but the location was arbitrarily shifted to the right to reduce overlap and make the shape clear. The FWHM of the spots are shown next to the off axis location. At the center, the spot size is 110 µm but it increases significantly once an off-axis beam is applied. For an input beam applied 12.7 mm off-axis, the spot size grows to 765 µm or about 10x larger. As the beam is applied farther off-axis,

the spot size continues to grow but not as large as the on-axis, off-axis change. The experiments were performed with the exposure set to make the intensity at the center near the maximum (4096) and this exposure was kept constant for all of the off-axis measurements. As is clear from Figure 6, the peak intensity drops rapidly with off-axis position and the width of the spot grows. The number of illuminated facets on the lens using the 4 mm laser width is about 30 for each of these measurements. For further discussion and comparison of the results of the spot size measurements, see Section entitled Discussion of Spot Size Measurements later in this report.

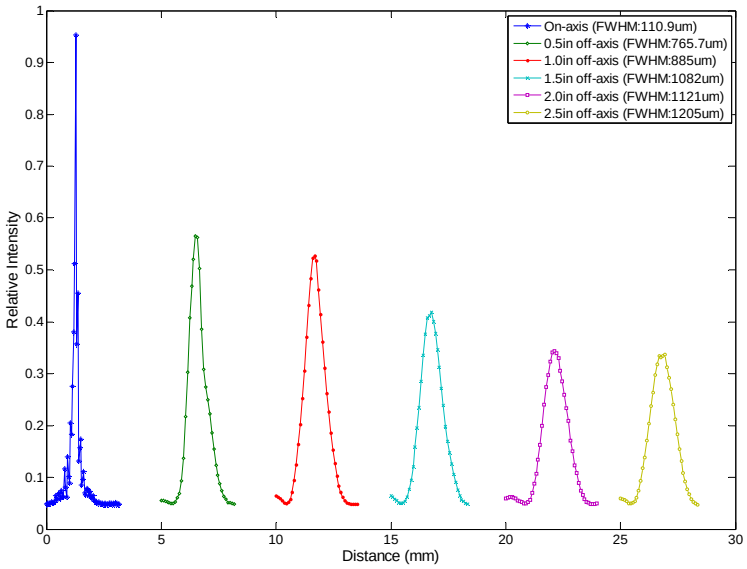

Figure 6. Measurement setup for the Fresnel focusing lenses and spot measurements for commercial Fresnel lens with 203 mm focal length both on and off axis. Distance off axis and corresponding spot sizes are shown in upper right.

5.6 ASPHERIC FRESNEL LENS

The spot pattern of the aspheric Fresnel lens was measured in the same way as the conical groove lens in the last section. The grooves face away from the camera with a 4 mm diameter solid state laser beam on-axis and at several off-axis positions.

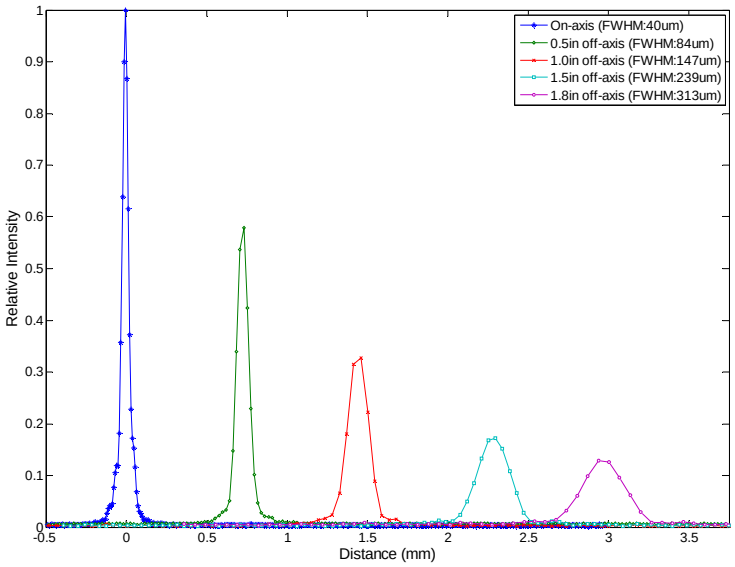

Figure 7. On axis and off axis spot sizes (data in upper left) for aspheric Fresnel lens.

Figure 7 shows the spot sizes measured for the different off-axis positions. The spot sizes for the aspheric lens are much smaller than the conical Fresnel lens ranging from 40 µm on-axis to 313 µm for a 46 mm (1.8 in) off-axis beam. Because of the increased width of the facets, fewer were illuminated for the 4 mm diameter laser beam; varying from 1 at the center to 7 for the 45 mm off-axis beam. For further discussion and comparison of the results of the spot size measurements, see Section entitled Discussion of Spot Size Measurements later in this report.

5.7 KINOFORM LENS

The spacing and angle of the facets on the Kinoform lens determine the location of the refractive and diffractive beams. For a phase match order of M = 1, the groove spacing must be very small at larger apertures and the lens becomes difficult to fabricate; for example, 6 µm spacing for a 200 mm f/l. lens at r = 11.5 mm. Even when the phase match order is increased to M = 5, the groove spacing is still very small. The lens cannot be contoured with a radiused tool as was done for the aspheric lens but rather must be machined as a series of plunge cuts. The side of the dead sharp tool forms the flat refractive portion of the lens and must be rotated at each plunge to change the angle as the groove radius is changed.

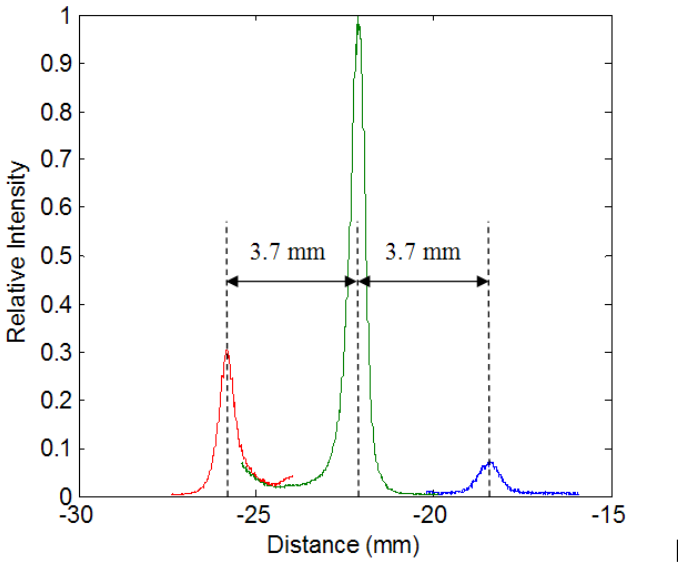

Figure 8. Kinoform Relative Intensity Plot, 190mm Focal Length. FWHM spot size at the central peak is 480 µm.

Spot Size Measurements The machined segment of a kinoform lens was used to measure the spot size in the same way as the conical and aspheric lenses. The collimated laser beam was directed into the kinoform lens (grooves away from source) and the camera was located near the designed 200 mm focal length. The spot consisted of a bright spot surrounded by a circle of lower intensity (~20%) with a radius of 3.7mm. The FWHM size of the central spot was 480 µm. The measurement shown in Figure 8 was created by moving the camera to make 3 images with the same exposure. Stitching them together provides a wider field of view than possible with the 4.5 mm focal array width. The image of the center was made and then the camera was translated left and right to add segments outside the field of view. The variation of the magnitude of the secondary peaks is probably caused by the alignment of the lens and camera. For further discussion and comparison of the results of the spot size measurements, see Section entitled Discussion of Spot Size Measurements later in this report.

The size of the spot from the kinoform was disappointingly large – nearly 0.5 mm. Since only an annular ring was machined, only one off axis segment (approximately 25 mm off-axis) could be measured. While a large spot, it is significantly better (half the size) than the commercial conical Fresnel lens (885 µm), but it is larger than the aspherical Fresnel lens (147 µm) machined at the PEC. Additional work related to the fabrication technique (ball bearing stage is potentially a problem) and lens design sensitivity studies will provide reasons for the measured performance.

5.8 DISCUSSION OF SPOT SIZE MEASUREMENTS

The size of the spots measured for the aspheric Fresnel lens was shown in Figure 7. The spot for the 38 mm (1.5 in) off-axis beam is reproduced in Figure 10. This has all the hallmarks of a diffraction pattern from a single slit. The experimental shape matches the shape from a 510 µm wide slit which is 203 mm from the camera. The shape of the aspheric lens at 38 mm from the axis is shown in Figure 10. If the assumption is made that the curved region of the Fresnel lens created by the tool radius does not play a role in the diffraction, the resulting width of the facets is 510 µm which agrees with the diffraction pattern that matches the data in Figure 9. This result was not expected but has some relevance to diffraction theory.

Based on the result for the 38 mm off-axis beam, the data from Figures 6 (conical Fresnel) and 7 (aspheric Fresnel) are compared in Figure 11. The data for the FWHM intensity from the spot measurement are shown as the markers and compare the results from the conic and aspheric lenses. While both lenses have small FWHM spots on-axis, each grow as the beam is moved off-axis. However, the aspheric lens is superior throughout the range. The steep increase in spot size for the conic Fresnel lens as the beam moves off-axis is dramatic.

The intensity of the diffracted light from a single linear slit can be estimated from Equation 1. This diffraction equation is written in a different form in Equation 2 with the variable $\beta = (\pi d \sin\theta)/\lambda$ where d is the width of the slit, λ is the wavelength (650 nm) and θ is the angle between the center of the slit and the location of interest at the camera.

$$I = I_0 \left(\frac{\sin\beta}{\beta} \right)^2 \qquad (2)$$

$$FWHM = \frac{2.783 \lambda y}{\pi d} \qquad (3)$$

In this form, the first zero for the function exists at $\beta = \pi$. It can also be used to find the value of I at the 0.5 or the half-maximum point. The 0.5 intensity occurs at $\beta =$ 1.39155. By using this value in the definition of β, an expression for the FWHM spot size for different slit (or facet) widths, d, can be written in Equation 3 where $y = \sqrt{\text{distance(off-axis)}^2 + \text{focal-length}^2}$; that is, the distance between the facet of interest and the focus of the lens.

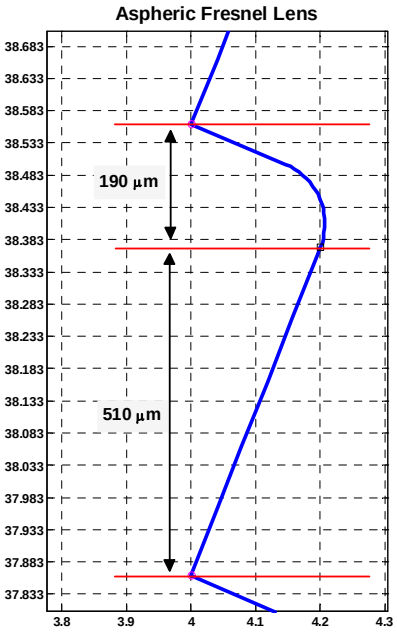

Figure 9. Section of two grooves of the aspheric Fresnel lens 38 mm off-axis. Note the 0.15 mm obscured region formed by the 0.1 mm radius tool and the relief angle.

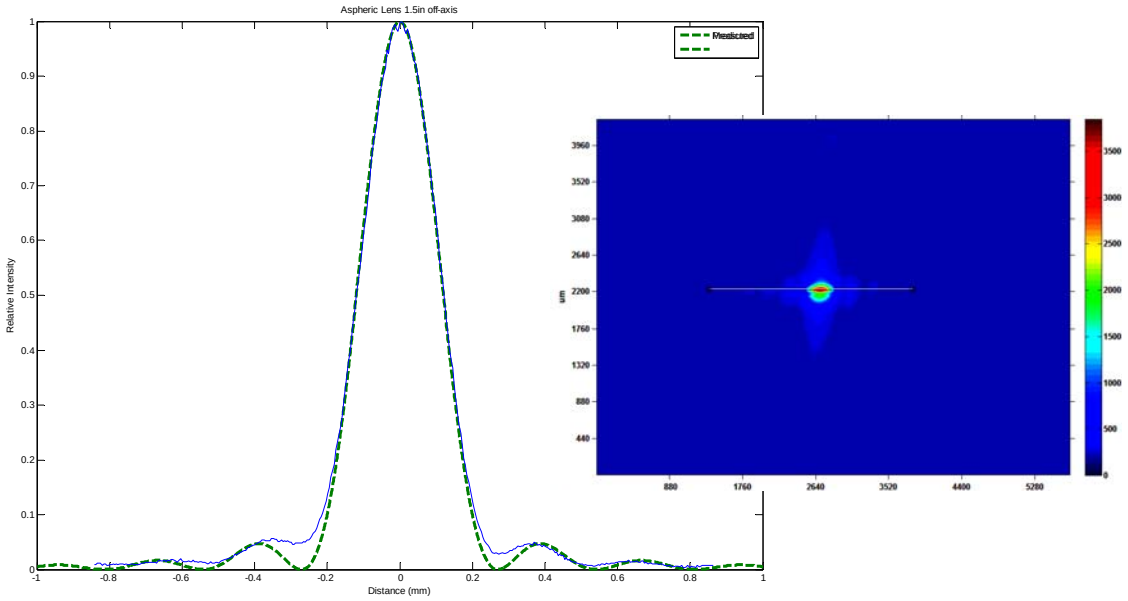

Figure 10. Spot size from 4 mm diameter laser beam 38 mm off-axis on the aspheric Fresnel lens. The diffraction pattern from a 510 μm wide slit 203 mm from the camera is also shown. Inset shows the 2D view of the spot and the line of the measurement.

The data in Figure 11 shows the FWHM values predicted for the conical and aspheric Fresnel lenses along with the measured values. The solid line is the predicted spot sizes for the aspheric lens based on the size of the facets less the width of the curved region caused by the tool nose radius shown in Figure 11. The results are surprisingly good and smoothly translate from on-axis values to the 45 mm off-axis values. The conclusion could be that the aspheric shape turns the light from each facet toward the focus but the diffraction from the boundaries increases the spot size as the size of the facets decreases.

The diffraction hypothesis that fit the aspheric lens data does not fit the spot sizes measured with the conical Fresnel data in Figure 11. For the conical Fresnel, the width of the facets is constant (127 μm) and the FWHM spot size prediction is nearly constant with off-axis distance. The prediction changes only because of the increase in distance from the off-axis point to the focus. There may be blocking of the facets as the off-axis distance increases that would reduce the "apparent" width of the slit and thus the spot size. This was not considered in the results shown in Figure 11 and no calculation was made to include the effect of blocked facets nor the effect of coherent superposition from the larger number of facets illuminated by the laser for the conical lens (31) compared to the aspheric lens (7 at the largest off-axis position).

The kinoform lens behaved much different than either the aspheric or conical lens. The kinoform is a conical lens but attempts to get all of the diffractive energy at (or near) the refractive peak. It has extremely small facet sizes (on the order of 33µm or 25% of the conical Fresnel) which will lead to large spot sizes from the diffraction model in Equation 17. The number of facets illuminated by the laser beam is much larger than the other lenses - on the order of 120. The predicted size of the spot at 25 mm would be 3.5 mm from the Equation 17 but the actual size was about 0.5 mm. This spot size is not as good as the aspheric lens but significantly better than the conical lens. The measurement of the lens facets pointed to variations in location on the order of a micrometer which is the order of the wavelength of the laser light. The sensitivity of this design to manufacturing tolerances is an important issue that should be addressed.

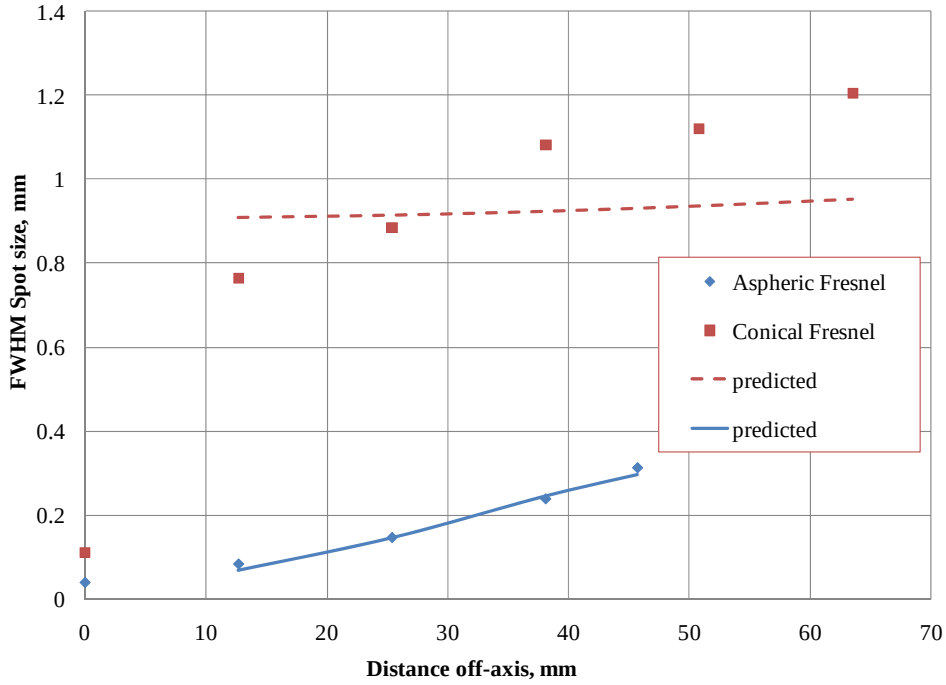

Figure 11. Full Width Half Maximum (FWHM) spot size vs. off-axis illumination distance. Data shown for aspheric Fresnel (lower) and conic Fresnel (upper).

5.9 CONCLUSIONS AND FUTURE WORK

An iterative aspheric zone Fresnel lens design code has been developed. The code includes toolpath generation and ray tracing through a simulated as-machined surface. A numerical diffraction analysis code for an arbitrary lens shape has been implemented. The code is general purpose in that aperture size, focal length and wavelength are not constrained. Extension of the routine to implement both refraction and diffraction through multiple surfaces is being implemented. A kinoform design code that matches the phase from adjacent Fresnel zones by

varying the zone width as a function of optical path length and wavelength has been written. The resulting lens directs both the diffracted and refracted light to the same locations, the focus. However the kinoform lens is very sensitive to wavelength changes and presumably manufacturing tolerances.

The testing of Fresnel lenses at the PEC has progressed from photographs made with a commercial SLR digital camera to a high-resolution, specialized monochrome array. While acquiring an understanding of the operation of digital cameras, both color and monochrome, a powerful tool for image analysis is now available for subsequent experiments and development. These techniques have been used to analyze the performance of slits, prisms, conical lenses, aspheric lenses and kinoform lenses. The results show great potential for using Fresnel lenses to focus sub-millimeter-size beams.

The measured and predicted spots for several commercial and custom fabricated lenses are discussed. The best performance came from an aspheric Fresnel lens fabricated at the PEC. Spots sizes measured ranged from 40 µm on-axis to 313 µm for a beam 45 mm off-axis beam. The spot size increase has been compared to the diffraction pattern for a slit equal to the facet size of the lens with impressive accuracy. The commercial conical and kinoform lenses did not show the same performance with spot sizes that were twice as large.

The lenses designed and fabricated thus far have been focusing Fresnel lens and the next logical step could be to design a scanning lens based on the lessons learned. A foundation has been created for understanding the operation of Fresnel lenses including refraction and diffraction. The discontinuous nature of the Fresnel-type surfaces presents unique design and fabrication challenges. This activity will add to the understanding of Fresnel design and how this type of lens might fit into a lens designer’s tool box.

6 DIAMOND TURNING OF SMALL SCALE ASPHERIC LENSES IN PMMA

Alex Sohn
Precision Engineering Center Staff

6.1 INTRODUCTION

Diamond turning of PMMA (Polymethyl-methacrylate) has been of importance to a number of industries and presents some unique challenges. While PMMA (also known by the trade names Plexiglas® and Lucite® as well as the generic term “acrylic”) has low shear strength, creating low cutting forces and, hence, long tool life, certain quasi-brittle behavior can cause surface finish issues. While this “tearout” or “zippering” phenomenon has been encountered before [1, 2], typically it can be avoided by using low feedrates and depths of cut. Achieving good surface figure also presents a unique challenge due to the low modulus of PMMA (2-3 Gpa) makes stress-free mounting difficult, particularly since blanks are not initially flat. The chief advantage of aspheric lenses is their ability to eliminate spherical aberration with a single surface whereas spherical lenses require multiple surfaces (usually three or more) to achieve the same result. This is of particular significance in instances where space or cost limits the application of doublet or triplet lenses such as CD/DVD lenses, cell phone camera lenses and ophthalmics. While most of these applications end up with molded lenses in the final product, prototype lenses for testing and development are typically machined directly from polymers such as PMMA. The objective of this project was to fabricate a set of aspheric lenses with an aperture diameter of 6 mm and an overall sag of up to 1 mm. A photograph of the lens is shown in Figure 1.

Figure 1. Photograph of the aspheric lens.

6.2 ASPHERIC LENS DESIGN AND TOOLPATH GENERATION

6.2.1 CALCULATING THE SHAPE

The aspheric shape of a lens is generally described by the general optics equation:

$$z = \frac{cr^2}{1+\sqrt{1-c^2(\kappa+1)r^2}} + dr^4 + er^6 + fr^8 + gr^{10}\cdots \quad (1)$$

Where z is the surface displacement, r is the radial coordinate along a meridian of the lens, c is the curvature of the lens, κ is the conic constant and $d, e, f\ldots$ are the higher-order aspheric terms. From this equation, data points along the lens's surface can be generated at an arbitrary interval. In order to maintain a good surface finish, the spacing of the data points must be chosen so that, with the lens's general curvature, the sag between each data point is less than the best achievable P-V surface finish. In this case, a value of 1 nm was chosen. With a general curvature c of $1/R$ where R=11.45 mm, the parabolic approximation can be used to estimate the points spacing d is

$$d = \sqrt{PV \cdot 8R} \quad (2)$$

Or in this case, the spacing shall be 9.57 µm. Since the lenses being fabricated have an aperture radius of 3 mm, this produces 300 data points total along the toolpath, not an unreasonable number. The data points were generated in Microsoft Excel and appended with code and feedrate information to allow interpretation by the PEC's ASG 2500 Diamond Turning Machine.

6.2.2 TOOL RADIUS COMPENSATION

Tool radius compensation must be performed to maintain the proper form of the part. There are two methods for performing tool radius compensation: 1) analytically derive an offset path one tool radius away from the original path or 2) find surface normals at given points along the toolpath and find new points offset by one tool radius in the normal direction. The latter was chosen here because the generated toolpath points are close enough together and the slope change between each set of surface points is small enough that the local slope can be approximated from neighboring points. Again, this action is simple enough that it was performed in Microsoft Excel. In this case, a 98 µm radius tool was used.

6.3 FABRICATION

With the toolpath generated, several fabrication issues loomed, the most significant being part mounting.

6.3.1 PART MOUNTING

For part mounting, three distinct possibilities exist: 1) Mechanical restraint, 2) Vacuum mounting

and 3) Adhesive mounting. The significant problem with PMMA and other polymers is that they have relatively low elastic moduli and are easily distorted even with small applied stresses. Because these parts are only 1-2 mm thick and the blanks do not start out flat it is difficult to securely mount the parts without distorting them. Both mechanical methods and vacuum were immediately dismissed for these reasons. With vacuum, the non-flat mounting face of the part is distorted into a flat shape so that if the part is faced off, it remains flat only for as long as it is held with vacuum.

The distortion above left bonding as the only viable mounting method. Bonding is, however not without its own problems, though as adhesive itself can distort the part, damage the mounting surface or leave residue that is difficult to remove. Optical mounting wax was tried initially since it conforms well to irregular surfaces and applies little stress. The relatively low melt temperature of the wax, 50ºC, should minimize thermals stress. However, in tests it was found that the process still induces too much thermal stress in PMMA to be useful, likely due to its high CTE. This is illustrated in Figure 2 with a measurement of residual error before and after mounting. While the part was flat before release from the wax, after release, the part exhibited a sag of 1.743 µm. This is a significant error for any optical component and greatly exceeds the tolerance of ±150 nm for the asphere parts. Similar tests performed with double-adhesive film tape revealed no residual stress and this method was thus chosen for mounting all samples.

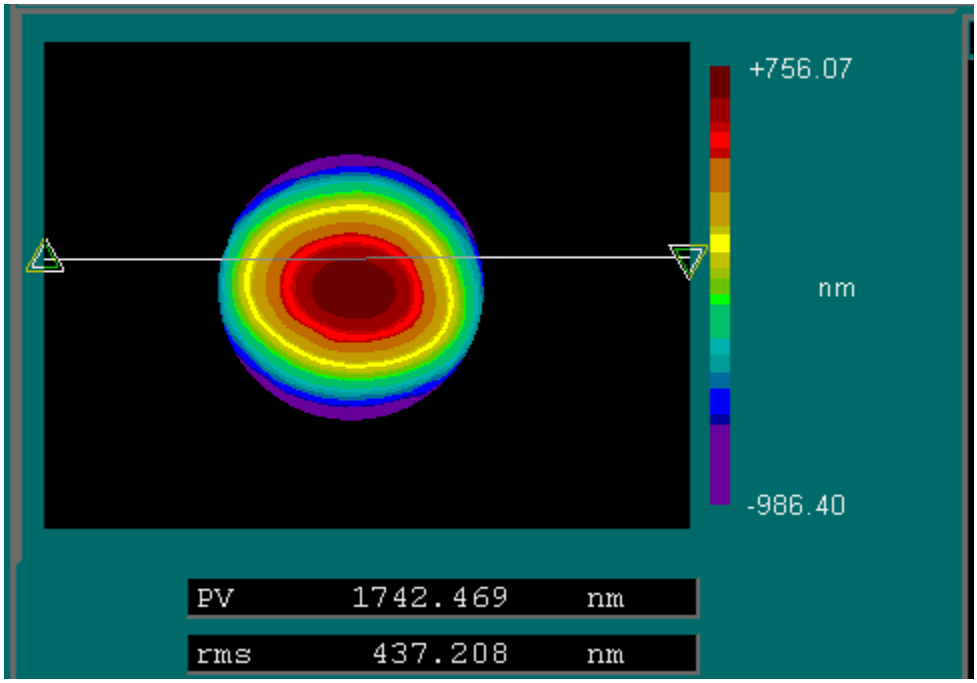

Figure 2. Residual error in plastic flat bonded to substrate with mounting wax after releasing.

6.3.2 TEST PART

Machining Test Sphere

Since the metrology of aspheres presents significant challenges, a spherical test part was chosen as a good independent indicator of the figure error that could be achieved in turning one of these parts. The radius of curvature was chosen to be the same as the base curvature of the aspheres to be machined, so that the only change between the test spheres and the final aspheres would be the conic constant. This would not only allow testing of the figure error with the Zygo GPI interferometer, but also the basis for compensation for systematic errors in the machining such as residual ogive, tool waviness and axis errors.

Error correction

The test sphere was measured using the Form Talysurf Profilometer as well as the Zygo GPI XP interferometer. The resulting errors come close to the tolerance of ±150 nm and, hence must be corrected. Shown in Figure 3, a polynomial is fit to the data points. This error, likely a caused by tool waviness, is then subtracted from the toolpath.

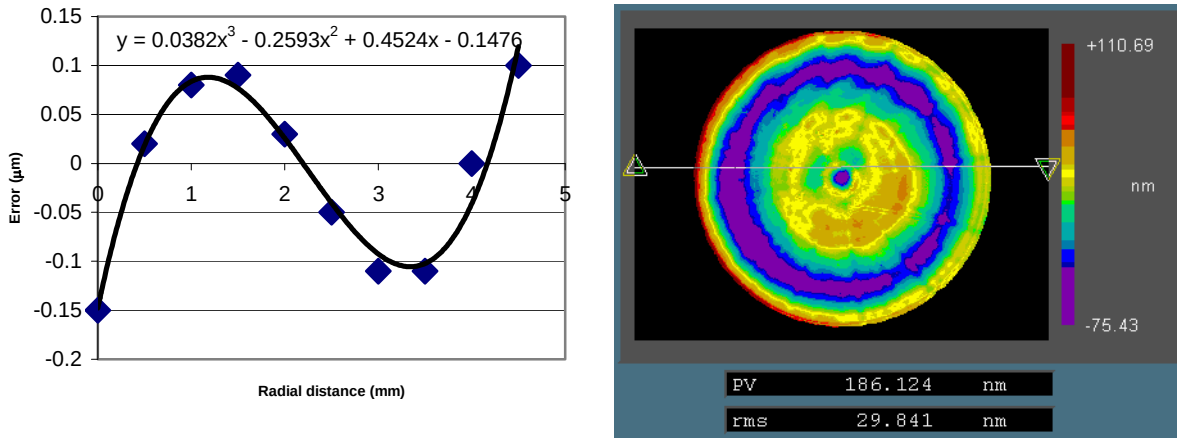

Figure 3. Polynomial fit to error data on a spherical test part (l.) and the resultant interferometry results after using the polynomial correction (r.).

6.3.3 MACHINING

With error correction applied, the aspheric lenses were machined using a cross-feed of 2.5 mm/min on the finish pass with a depth of cut of 2 µm. Cuts were performed dry with ionized air used to remove chips. The ionization prevents static discharge which is potentially damaging to the tool and static attraction of the chip to the part. All parts were faced on one side to achieve

a flat back surface and then re-mounted using the double-stick adhesive tape to contour the aspheric face.

6.4 METROLOGY

6.4.1 SURFACE FINISH

Given a theoretical surface finish of 1 nm RMS, the actual surface finish of between 5 and 6 nm RMS measured on all samples was quite satisfactory. Shown in Figure 4 is the result of one such measurement performed with a Zygo New View 5000 Scanning white-light interferometric microscope. This surface finish is typical of the best finishes that have been achieved in PMMA on the ASG 2500 [1] and appears to be mainly limited by the material as evidenced by the irregular tooling marks on the surface.

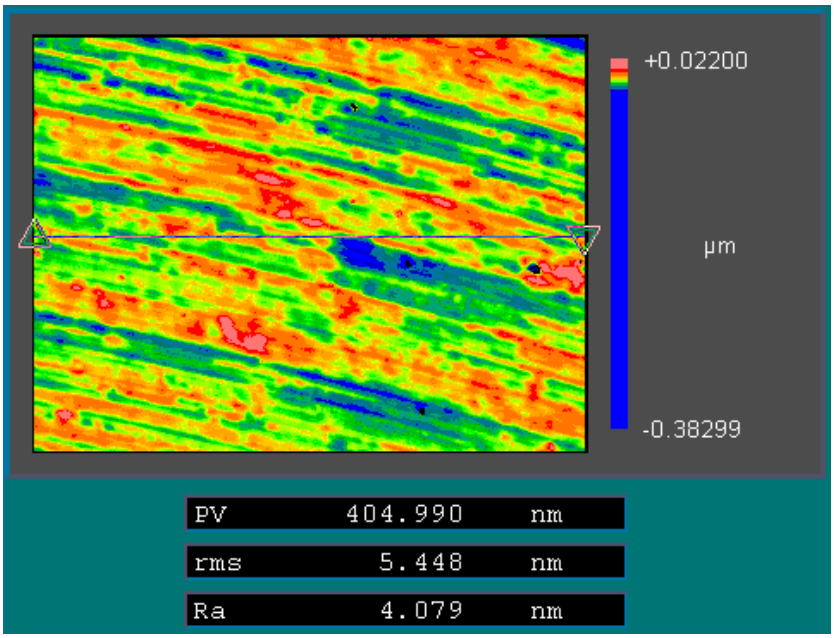

Figure 4. Typical surface finish measurement for one of the aspheric PMMA lenses.

6.4.2 FIGURE MEASUREMENT

Final figure measurements could not be performed with an interferometer due to the aspheric nature of the lenses, so the PEC's Form Talysurf was used for measurement and analysis. The stylus profilometer was used to measure one meridonal trace for each lens. Since the aspheres measured only consisted of conic constants and no higher order order terms, they were actually ellipsoidal with conic constants ranging from +0.52 to -0.13. This means that the Talysurf's

fitting routine for ellipses and hyperbolae could be used. The result of these fits produce an output of major and minor axis dimensions *a* and *b*. From the values of *a* and *b*, the conic constant, k and radius can be calculated.

$$\kappa = \frac{b^2 - a^2}{a^2}, \qquad R = b(\kappa + 1) \tag{3}$$

Residual errors were below the target uncertainty of ±150 nm. Figure 5 shows the residual error is well within the specified limit and is typical of the types of error measured on all of the PMMA lenses.

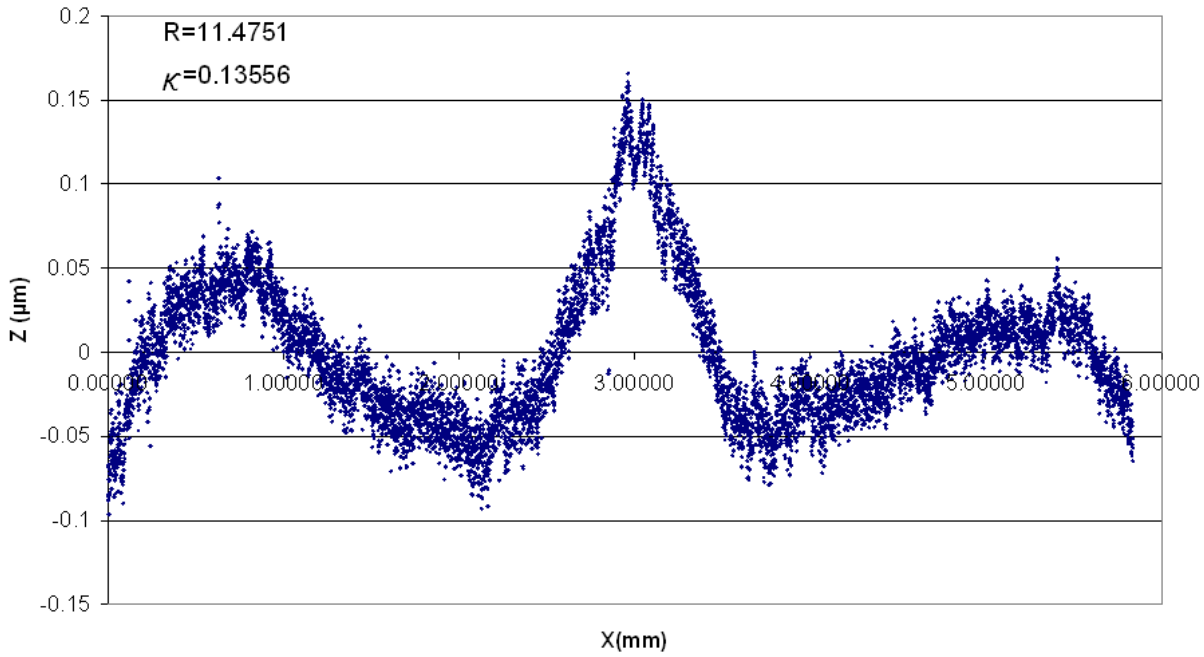

Figure 5. Figure error measurement for an aspheric lens. Peak-to-Valley error was measured at 265 nm with the best-fit ellipse removed from the data.

6.5 CONCLUSIONS

This work represents a practical look at machining aspheric surfaces in PMMA. In general, the lessons learned apply to all instances where easily deformed parts must be securely mounted and where distortion can play a significant role. In this case, the traditional vacuum mounting techniques do not work well anymore and are replaced by the use of adhesive that applies substantially less stress to the part. It has also been demonstrated that systematic, repeatable machining errors such as tool waviness, axis errors, etc. can be removed from the part without regard to their source. In the end, high-tolerance PMMA lenses can be directly machined for prototype work.

REFERENCES

1. A. Sohn, K.P. Garrard, and T.A. Dow, *Fabrication of Non-Imaging Optical Surfaces.* PEC Annual Report 1998, pp 207, (1998).
2. A. Kobayashi, Machining of Plastics, Robert E Krieger, New York pp 59ff, (1981).

7 POLARIS MECHANICAL DESIGN

Alex Sohn
Precision Engineering Center Staff
Karl Falter
Consultant

7.1 INTRODUCTION

In 2001, the PEC designed, fabricated and delivered a 2D polar profilometer for Vistakon to measure brass contact lens molds. The machine performed well with 100 nm accuracy but the user interface made it decidedly slow and difficult to use. In addition to the user interface, two other drawbacks of this design were the contacting probe and the 2D measurement capability. Based on the success of the prototype, an industrial partner was identified, a patent application was submitted and approved [1] and the development of a commercial prototype was begun. Unfortunately changes in business strategy at the industrial partner stymied further development and the unfinished commercial prototype was shipped to the PEC. The original prototype is in storage at Vistakon. Because the Polaris is such an ideal geometry to measure the small, high aspect ratio optical surfaces, the commercial prototype is being revived and converted to allow non-contact, 3D measurements contact lens molds. The modifications include a chromatic aberration optical probe, a rotary part stage and a linear axis to locate the part. The extension of the high-precision instrument for measuring aspheric and non-rotationally symmetric optics will expand its measurement capability and range of industrial usefulness.

7.2 OPTICAL PROBE

The optical probe used in the 3D Polaris works on the principle of chromatic aberration for distance measurement. Chromatic aberration is normally an undesirable defect in optical systems that causes light of different wavelengths to be focused a different distance from the lens as shown in Figure 1. The reason for this effect is that dispersion rates in most materials vary somewhat with wavelength with longer wavelengths effectively being refracted less than shorter wavelengths. As shown in Figure 1, the probe focuses white light into a spot. The reflected light is then collected by the probe and sent to a spectrometer. The distance at which the light is focused depends upon wavelength or color since the lens is designed to display a certain degree of chromatic aberration. The spectrometer thus sees a peak in reflectance at a wavelength that varies as a function of distance.

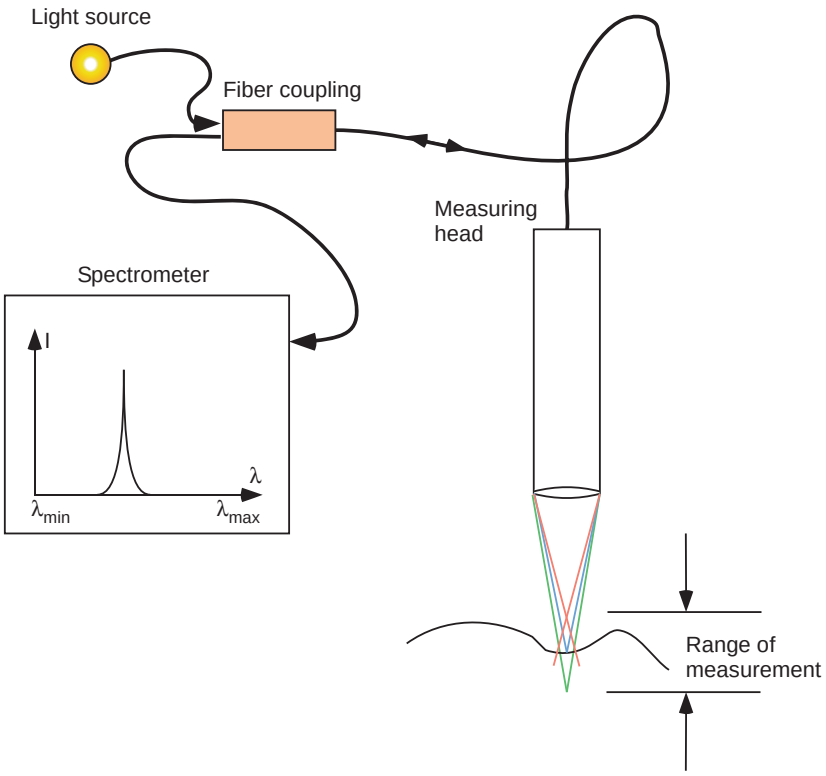

Figure 1. Light of different wavelengths has varying focal lengths when chromatic aberration is present.

One significant advantage of the chromatic aberration probe is that the frequency component of the reflected light changes very little as a function of angle of incidence. This allows the probe to operate even when it is not normal to the surface being measured. Given the aforementioned characteristics and the capability to operate at 1 kHz, a CA probe manufactured by Stil S.A. has been obtained from Vistakon to be tested on the Polaris system. The model chosen has a 300 µm displacement range and ±25º angular range.

7.3 ADDITIONAL AXES

Two additional measurement axes are being added to the existing Polaris to extend operation to three dimensions. As shown in Figure 2, the θ and R axes used in the 2D version of Polaris are supplemented with φ and Z axes. Both axes are air-bearing brushless motor driven axes with high-resolution encoder feedback. The linear axis is an Aerotech ABL 1000 with 100 mm of travel and a resolution 0.5 nm. The rotary stage is an Aerotech ABRT-150 with a 100 mm table diameter and a resolution 0.055 arcsec. The Z-axis is not considered a measurement axis since it is to remain stationary during measurement, but its straightness is critical to maintain the correct relationship between the measurement axes, φ, θ and R. This is the reason for the selection of the air-bearing stage.

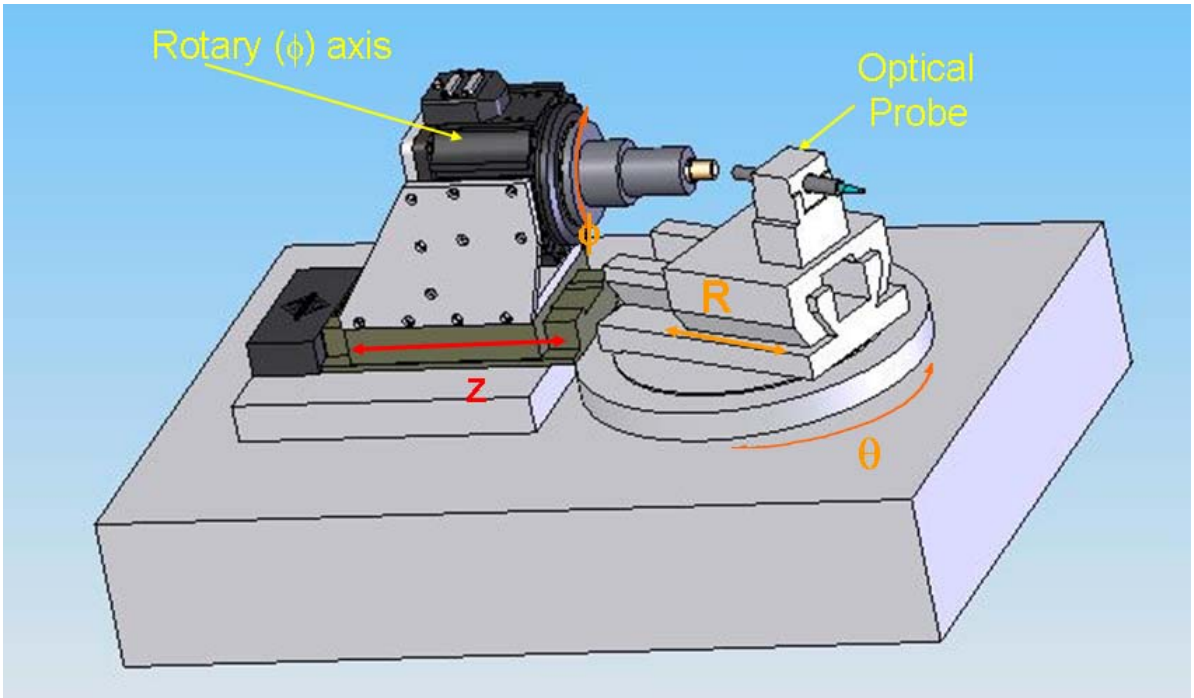

Figure 2. Axis Layout of final Polaris version showing new φ and Z axes and location of optical probe.

7.3.1 MACHINE DESIGN

The new machine axes have been chosen and mountings designed to meet several requirements. The linear Z-axis was mainly chosen for its travel (100 mm) and load capacity. The combination of the rotary φ axis, mounting plates and part chuck have a combined mass of 10 kg, well within the stated 15 kg load capacity of the Aerotech ABL-1000 air-bearing stage. Since it is mounted with its axis horizontal the load requirements for the φ axis are based on a moment due to the cantilevered load of the part chuck and part. Given a mass of 1.8 kg for the part chuck, and a distance of 113 mm from the spindle air bearing center to the chuck center of mass, the moment is approximately 2 N-m, well below the specified 3.5 N-m tilt load limit of the Aerotech ABRT-150 unit selected. In addition to load requirements, straightness, angular errors and runout specs had to be met. The mounting plates will place the φ-axis spindle close to the correct height with enough play in the fasteners to allow fine-tuning the height. The mounting plates also have to locate the spindle correctly in the Z-direction to allow use of the full measurement range but also provide enough clearance between the components. A feed-thru will be fabricated to allow actuation of the air-operated collet chuck for holding parts.

7.3.2 MACHINE ASSEMBLY

During assembly, the new axes will be aligned with the other axes to maintain the spherical coordinate system upon which measurements will be based. Procedures for performing these alignments have been developed to assuring that a) the φ and θ axes intersect at a right angle, b) the R and φ axes are collinear at θ = 0, r and θ axes are perpendicular and c) the φ and Z axes are collinear.

7.3.3 PRELIMINARY TEST SETUP

Due to the 2 month lead time on the new rotary and linear axes, a preliminary test setup using a Professional Instruments 4R air bearing spindle, a dc motor and a 7200 counts/rev angular encoder has been created. The motorized spindle is mounted atop the existing stepper motor X and Z axes of the 2D Polaris machine as shown in Figure 3. While position resolution and straightness are not up to final specification, the setup is sufficient to test alignment techniques and demonstrate the data collection from the optical probe and 3D shape measurement techniques.

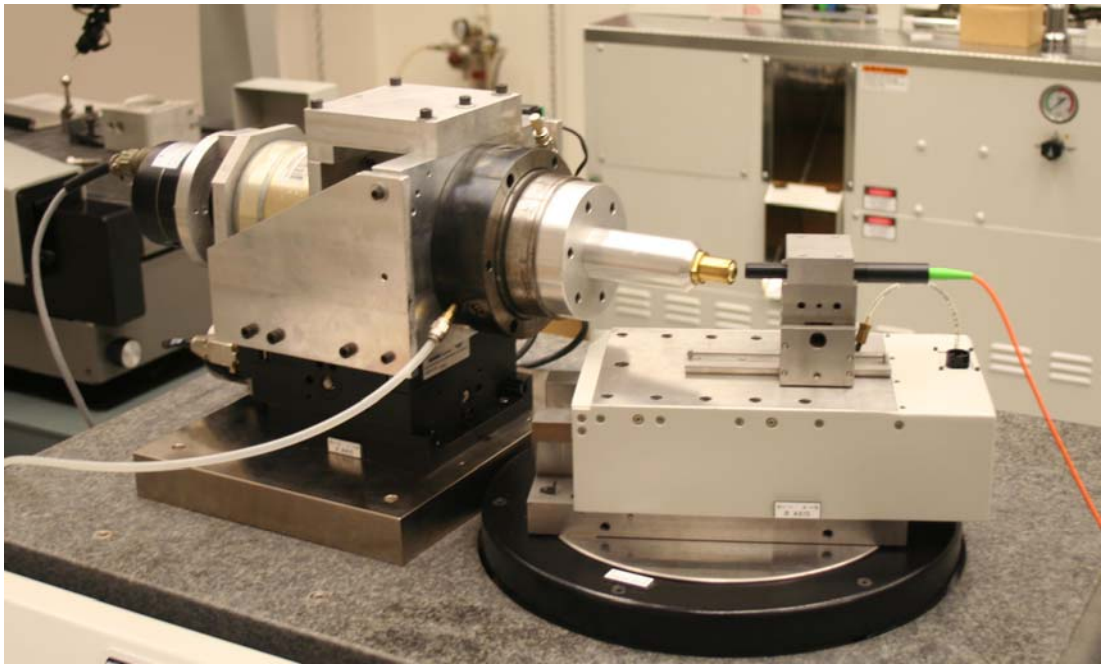

Figure 3. Test setup showing the provisional φ axis holding a test sample

7.4 CONCLUSIONS

This project began in the late spring and it is progressing at a rapid pace. The final layout of the machine has been determined and the usefulness of the optical probe demonstrated. The test setup is complete and allows testing of the more complex tasks involved in making 3D measurement of a contact lens mold. With continued development, it will be shown that Polaris 3D can be used in a broad range of applications including DVD lenses, ophthalmic, prosthetic joints, diesel engine lifter cups and many more.

REFERENCES

1. A. Sohn, K. P. Garrard, T. A. Dow, *The Polar Profilometer Polaris*, Proceedings of ASPE, Vol 25, pg 28-31, 2001.
2. A. Sohn, K. P. Garrard, T. A. Dow, *US Pat No 6895682: Polar coordinate-based profilometer and methods*, Nov. 2002.

8 POLARIS 3D OPERATION AND CONTROL

Kenneth Garrard
Precision Engineering Center Staff
Amir Pirzadeh
Tisfoon Ulterior Systems, Cary NC

8.1 INTRODUCTION

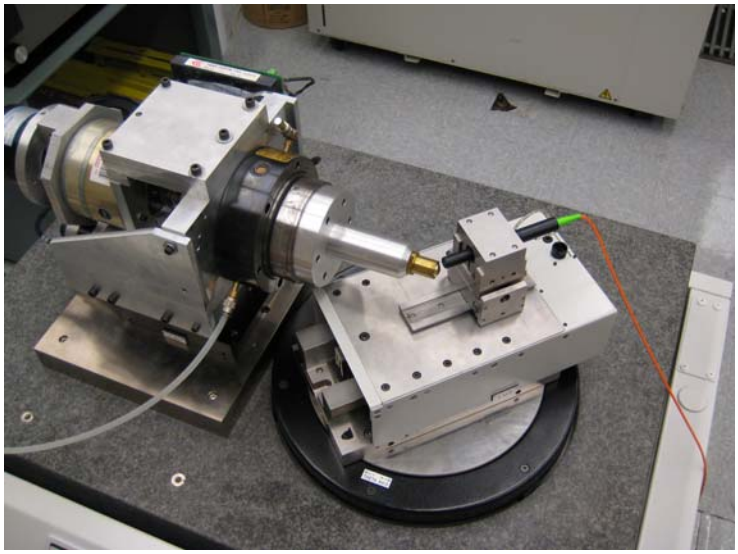

Figure 1. Polaris 3D.

The polar geometry measuring machine developed in by the PEC in 2000 [1-5] is being upgraded with an additional rotary axis and linear axis to create a 3D spherical coordinate measuring instrument. While awaiting delivery of new linear and rotary axes a temporary rotary axis has been interfaced to the Polaris 2D machine at the PEC to support controller and operating procedure development. Shown in Figure 1 are two opposing sets of stacked axes; linear on top of rotary with a vertical axis of rotation (R and θ) and rotary on top of linear with a horizontal axis of rotation (X, Z and φ). The measuring probe is mounted on the linear R axis. As a part is rotated in a vertical plane by the second set of axes arcuate motion of the probe in an orthogonal horizontal plane allows a spiral set of data to be collected and assembled into a 3D surface profile.

8.2 STIL CHR 150 OPTICAL PROBE

Non-contract metrology for Polaris 3D is desirable to avoid damage to finished optical surfaces. A STIL CHR 150 optical probe is available for this project. In this probe an axially chromatic lens and double spatial filter is used to produce a confocal imaging system for distance measurement. For any probe lens to object distance, light of a specific wavelength (i.e., color) will be in focus. The CHR 150 has a spot size of 8 μm and a maximum measurement range of 300 μm at a working distance of 5 mm. Its axial accuracy is 90 nm and lateral resolution is 4

μm. The steepest slope that can be measured from a specular surface is 25°, although this value is highly dependent on material and surface characteristics. The output of the probe controller is a unipolar 10 volt analog signal linearly scaled into the adjustable measurement range. A second analog output (also 0 to +10 volts) is proportional to the intensity of the measurement signal. The probe bandwidth is 1 kHz.

The measurement signal voltage increases as the distance from the probe to the surface increases. The intensity signal represents the "quality" of the reflected light and decreases as the probe is moved closer to the sample or as the slope is increased. A highly specular surface may saturate the detector or there may not be enough returned light from a diffuse or rough surface. Both the intensity and displacement output voltages are zero when the probe is too close or too far from a reflective surface or if there is too much reflected light or not enough reflected light. Changes in specularity, scratches and sharp slope changes may all result in the loss of a signal from the probe.

It is desirable to use the probe not only as a measurement device, but for the machine controller to use the probe as a secondary feedback source such that the machine axes "follow" the probe. This will enable the measurement of complex surfaces without programming the machine axes to move in a trajectory that follows the shape of each part.

8.3 UMAC CONTROLLER

The Delta Tau UMAC controller embedded in the prototype Polaris 2D machine (see Figure 2) has been upgraded for Polaris 3D. A PC/104 single board computer has been added to the UMAC card cage, eliminating the need for a separate PC host. This should also speed up data transfer between the UMAC and the user interface software by utilizing bus communications instead of USB or RS-232 serial. Additionally a high resolution sine/cosine interpolator board will be added to the UMAC to process analog encoder feedback signals from the new rotary (φ) and linear (Z) axes.

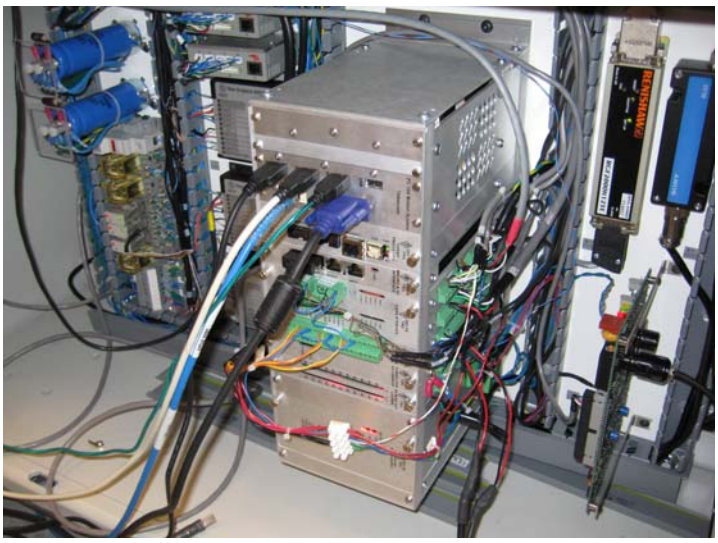

Figure 2. UMAC Controller.

8.3.1 SERVO CONTROL AND PLCS

The UMAC is responsible for motion control of all axes (R, θ, Z and φ) and data acquisition during part setup,

calibration and measurement. Software PLCs are used to home the axes and to detect faults and respond appropriately (e.g., stop motion if an axis is moved beyond its range). The UMAC is not programmed as a general purpose computer to control the machine axes. Rather the servo code (PID plus acceleration and velocity feedforward) and motion program interpreter are embedded in firmware and the user/OEM specifies operating modes, a mapping of the machine geometry to a coordinate system, controller gains and the I/O configuration. The firmware performs trajectory generation along a specified path through Cartesian space and servo control for the motors as a high priority real time task. Background processing (i.e., while waiting for the next real time interrupt) includes responding to commands from a host computer, reporting motor positions, machine fault detection and other housekeeping tasks. These later functions are implemented as software PLCs (programmable logic controllers). Table 1 lists the Polaris 3D PLCs and their function.

Table 1. Polaris 3D Software PLCs.

PLC	Function
estop	Initializes the controller, establishes communication with the user interface and starts other PLCs. Monitors machine state for errors and stops axis motion if there is a fault.
axpos	Reads axes positions and reports to the user interface. Monitors the overtravel status of all axes and implements a probe filter to quantify signal integrity.
psetup	Implements probe setup procedure and data analysis.
trigger	Moves one of the linear axes until the probe is in range.
probetrack	Continuously tracks probe position and commands the R axis servo filter to follow the probe. Records measurement data in a circular queue for the user interface. This high priority PLC executes once per servo update cycle.
jog	Commands axes to move in response to user input via axis and speed selector switches and the handwheel.
homeR, homeTheta, homeZ, homePhi	Move axes to their home position and initializes the machine coordinate system.

Probe signal integrity

The STIL probe measures the change in distance between the probe pen and a reflective surface. If the probe-sample distance is not within the working range (5000±300 μm) both output voltages (distance and intensity) will be zero and the probe is out-of-range. However, it has been

observed that when the probe sample distance dithers near either edge of the measurement range any signal voltage is possible. Filtering can reduce, but not eliminate, the likelihood of incorrectly deducing overtravel from the time history of probe signals. These signals can be zero for a variety of reasons not related to displacement and the probe can be crashed into a sample while still generating valid measurement data. For these reasons the probe signals will not used for overtravel detection. Instead the integrity of the probe data is monitored by the position reporting PLC, `axpos`, which will halt measurement if too much data is lost. The threshold for halting a measurement will be determined by the nominal part geometry, initial intensity recorded during part setup, angular range of the measurement and a user specified tolerance for missing data.

R Axis control with optical probe input

The R axis has two operating modes. It can be commanded moved independently of the other machine axes either from the user interface or with the manual handwheel controls. Alternatively the servo control loop for R can consider the optical probe measurement signal as an error that should be driven to some setpoint (e.g., 0 volts) by moving the axis. This type of feedback loop is easily implemented on the UMAC controller using the real time software PLC, `probetrack`, to filter the probe signal before it is scaled and saved for the R axis servo loop. The PLC also includes a rate limiter that prevents axis oscillation in response to analog noise and it ceases to update the control command if the probe signal is not "good". Thus the R axis will complete the accumulated command and simply stop moving if the probe signal is lost. In the worst case of a rapidly changing probe signal that moves through its full range in one servo cycle the R axis will move no more than 150 μm trying to respond to the probe. The control action for this follower servo loop is intentionally weak so that the R axis is stable, yet the steady state error is less than 20 μm. Thus less than 10% of the probe range will be used during a measurement.

8.3.2 USER INTERFACE

A consultant, Tisfoon Ulterior Systems, has been contracted to assist with controller integration and prototype user interface programming. Development of a full user interface is not part of the current project, however a host PC interface is needed to operate the machine and store measurement data. The tools provided by Delta Tau, PEWIN and PMACPLOT, are sufficient, but cumbersome to use and error prone. Tisfoon Systems has developed a highly flexible application that provides similar functionally in an easier to use format. Figure 3 shows the basic screen layout of this interface. Customization of buttons, dialogs, data entry, display and data acquisition functions will be performed as the system requirements evolve.

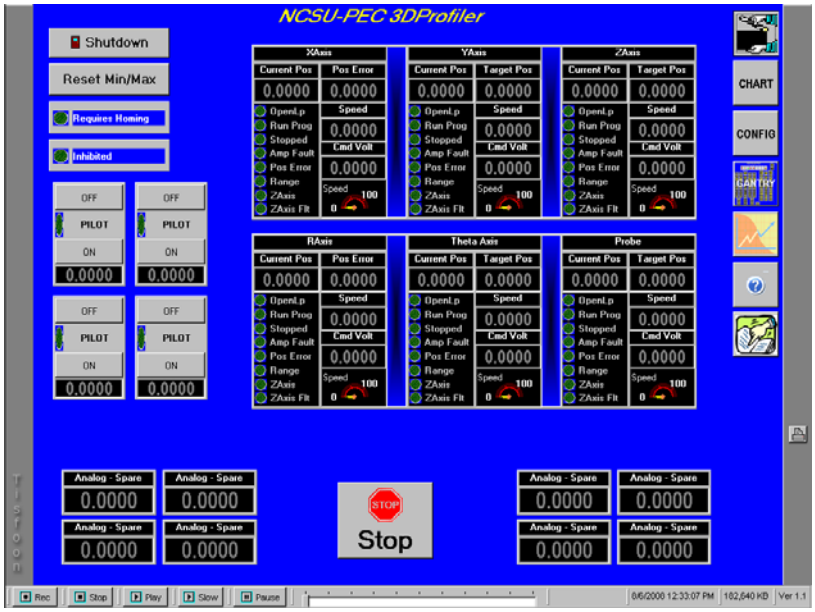

Figure 3. Prototype Polaris 3D User Interface

8.3.3 DATA ACQUISITION

Synchronized, real time data acquisition of probe and axis position data during a measurement is critical to the success of the project. To rapidly measure a nominally spherical part in a few minutes with dense point spacing on the surface the full probe bandwidth must be used and data collected at 1 kHz. The UMAC does not have enough memory to store a full data set so a region of memory has been reserved to implement a circular queue with a real time UMAC task filling the queue at one "end" while the TDProfiler application on the host PC/104 reads data from the other "end" of the queue and saves it to the disk drive. In this way the rates at which data is stored and data is retrieved do not have to match as long as the long term average rate of the reader is as fast as the writer. A larger queue allows for greater variance in the rate. The amount of data transferred is greatly reduced by saving the difference between successive values in the queue and performing a cumulative summing operation to recover the original data. This is most effective for fast collection of slowing changing large values such as encoder feedback from a slowly rotating axis acquired at 1 kHz.

The current implementation of this reader-writer scheme for data acquisition is simple to program and works, but it not fast enough. Several more complex software methods are being evaluated such as reading data in larger units, saving the data as binary instead of ascii and converted after a measurement is complete. Another solution is to purchase a UMAC controller card with sufficient RAM to save an entire measurement. The user interface can begin retrieving data as soon as measurement starts, but would not have to keep up with the acquisition process.

8.4 INITIAL RESULTS

The prototype machine is operational with a temporary part spindle (φ) and incomplete user interface. The axes have not been aligned nor have there error motions been fully characterized. However, the performance of the optical probe is being evaluated using two different types of surfaces: a flat and an asphere.

8.4.1 PROBE SETUP WITH A FLAT

Setup of the probe on the R axis requires knowledge of its alignment with the motion of that axis and the rotary table that supports it (θ). As outlined in [1] part of this process is establishing the origin of the linear translating axis pair (R and the probe) with respect to the rotary table. The goal is to find a point in the travel of the R axis such that as the table rotates the focused beam from the optical probe is stationary. This point in space can be considered the origin of the R–θ polar coordinate system and is the origin of the R–θ–φ spherical coordinate system as well if the θ and φ axes intersect at this same point. Equation 1 describes the displacement measured by the probe as a function of rotary axis position (θ), linear offset in the measurement direction (ρ_0) and linear offset tangential to the measurement direction (τ_0) if a flat surface is positioned in the measurement range of the probe and is perpendicular to the R axis motion at θ = 0°

$$\rho = \rho_0\left(\frac{1}{\cos\theta} - 1\right) + \tau_0 \tan\theta \tag{1}$$

The two unknown offsets, ρ_0 and τ_0 are zero then the probe is perfectly aligned. These offsets can be found by making two measurements at opposite angles of the flat surface, R1 and R2. Since the error due to ρ_0 is an even function it will not change in magnitude or sign. The error due to τ_0 will have the same magnitude but opposite sign. Thus the two offsets can be calculated from two measurements, R1 at θ and R2 at -θ, using Equations 2 and 3.

$$R1 + R2 = 2\rho_0\left(\frac{1}{\cos\theta} - 1\right) \tag{2}$$

$$R1 - R2 = 2\tau_0 \tan\theta \tag{3}$$

Figure 5 shows the results of measuring a nominally centered flat in both Cartesian and polar coordinates. The plots show the combined value of R plus the probe distance signal while θ was rotated 20°. The green trace is the uncorrected data and shows that there is a τ direction offset. The ρ offset is zero. The value of τ_0 can be found from Equation 3 using any two data points at opposite angles (e.g., ±9.9°). Alternatively the parameter could be found by performing a least

squares fit of the tangent function to the data points or an average value could be used. The plot shows the corrected data (red trace) using a value of -7.4 μm for τ_0.

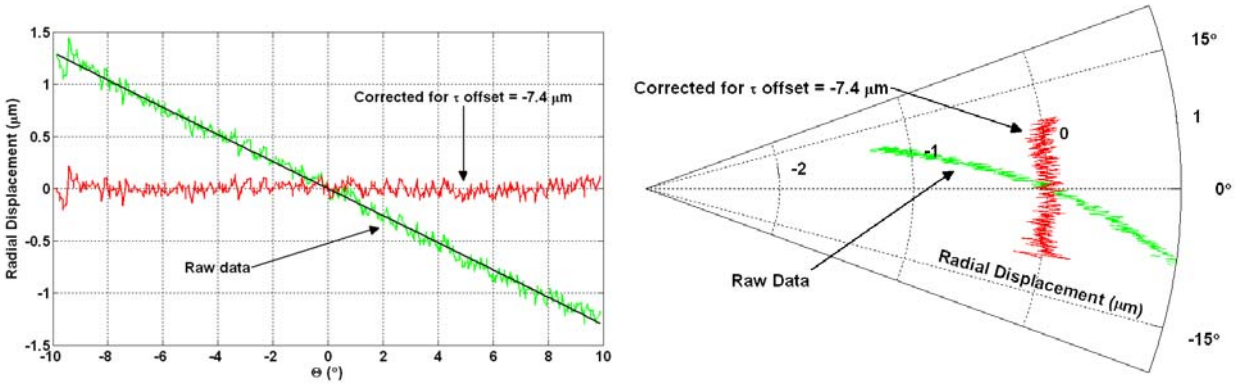

(a) rectangular coordinates (b) polar coordinates

Figure 4. Polaris measurement of a flat shows the tangential direction probe offset.

8.4.2 ASPHERE MEASUREMENT

A cross-section of an aspheric surface has also been measured with the prototype 3D machine using the coordinate origin and offsets found from the flat part measurement discussed above. Figure 5 shows the probe and part during the measurement. The table was rotated 90° while the R axis probe following was used to keep the probe distance signal near the center of its range. Data was collected at about 100 Hz. The intensity signal from the probe is shown in Figure 6a. There was a significant surface slope near the extreme edges of the part resulting but the central ±30° region the incident beam of the probe was nearly normal. Data points with intensity values below 8% were eliminated before further processing.

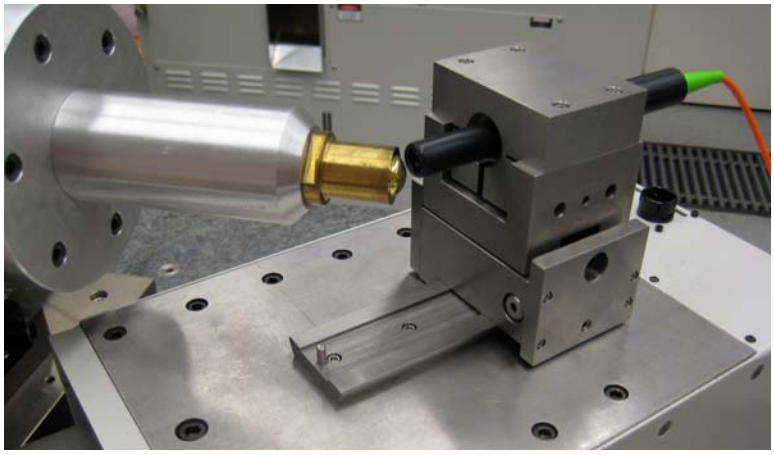

Figure 5. Measuring an asphere.

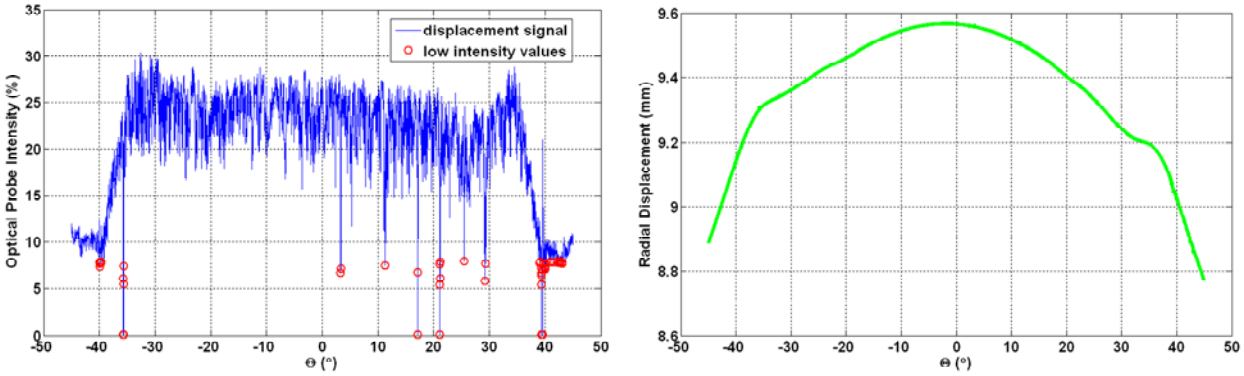

(a) Intensity signal (b) Surface cross-section

Figure 6. Asphere measurement data.

The assembled measurement is shown in Figure 6b. The R axis position and the corrected probe readings have been summed to obtain the trace in the plot. Figure 7 shows the same data set in Cartesian (7a) and polar coordinates (7b) along with two least squares circles; one with the center constrained to the origin of the coordinate system (which is coincident with the rotational axis of θ) and the other with no constraints.

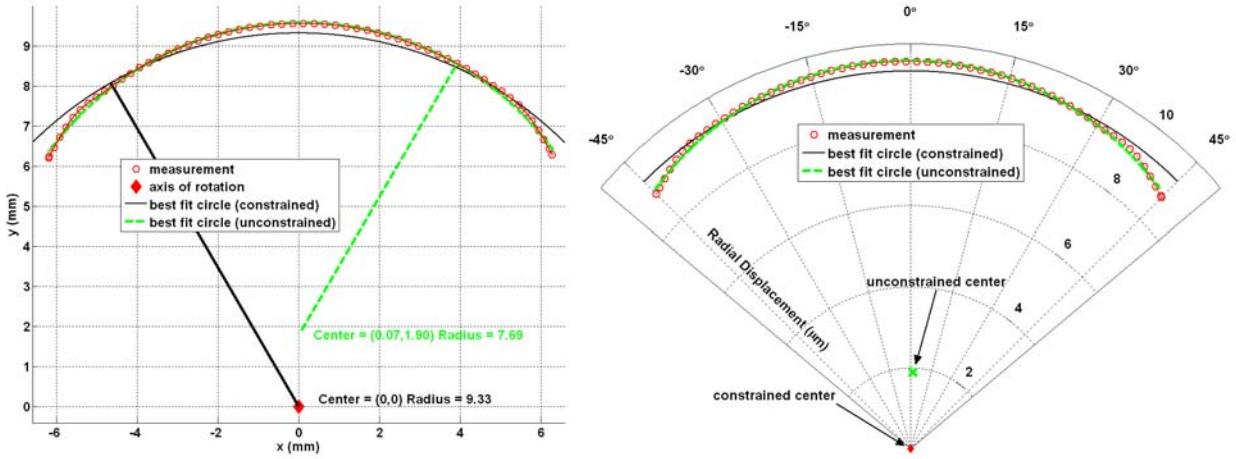

(a) Cartesian coordinates (b) polar coordinates

Figure 7. Asphere cross-sections and least squares circles.

The residual radial errors from the two curve fits shown in Figure 7 are plotted in Figure 8. The fit to the unconstrained circle shows that the central region of the part is nearly spherical. The outermost region also appears to be spherical but with a much smaller radius.

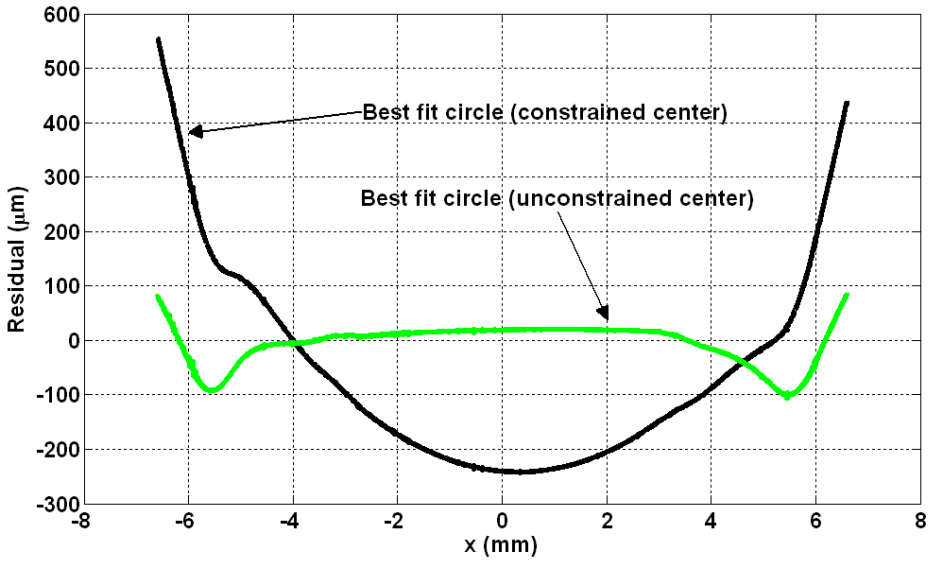

Figure 8. Asphere residual after least squares fit.

8.5 CONCLUSIONS AND FUTURE WORK

The Polaris 2D machine has been converted into a prototype Polaris 3D machine. This temporary configuration is useful as a test bed for the development of operating procedures, collection of axis error motion and calibration data. The control system hardware is nearly complete and a workable user interface has been constructed. The STIL optical probe has been interfaced to the controller and a general probe following servo algorithm has been implemented. Further analysis of the probe signals with varying surface properties and incidence angles is needed.

REFERENCES

1. Sohn, A. and K. Garrard. The Polar Profilometer *Polaris*. Precision Engineering Center Annual Report, 19, 1-16, North Carolina State University (2001).
2. Sohn, A., K. Garrard, T. Dow. The Polar Profilometer "Polaris." Proceedings of the Sixteenth Annual Meeting of the ASPE, 25, 28-31 (2001).
3. Sohn, A., K. Garrard, T. Dow. Ultraform 2D. Precision Engineering Center Annual Report, 21, 45-60 (2003).
4. A. Sohn and K.P. Garrard. Tip Waviness Compensation in a Polar Profilometer. Proceedings of the Eighteenth Annual Meeting of the ASPE, 30, 355-358, (2003).
5. United States Patent 6,895,682. Polar coordinate-based profilometer and methods, May 24, 2005. Alexander Sohn, Kenneth P. Garrard and Thomas A. Dow.

9 AUTOMATED HANDLING TECHNOLOGY FOR PRECISION TWO-SIDED PARTS

Stephen J. Furst
Graduate Student
Thomas Dow
Dean F. Duncan Distinguished Professor in Mechanical Engineering
Department of Mechanical and Aerospace Engineering

9.1 INTRODUCTION

The challenge of aligning a part on a lathe is relevant to many turning operations, including the fabrication of two-sided parts on a precision machining station. When machining a two-sided part such as a hemishell, one side is machined first. Then the part must be taken off the first holding fixture (typically a vacuum chuck), rotated, and replaced on another fixture that is suited for machining side two. During this transfer, the part becomes misaligned, and features on side two will not be properly related to features on side one.

The goal of this project is to automate both the part transfer and alignment steps required for fabrication of a hemishell. Currently, the part is transferred by hand, and realignment involves an operator measuring the part run-out with a displacement gage then manually tapping the high side of the part until it is centered. The actuation method must capable of correcting radial run-out of up to 2.5 mm to within 5 μm.

9.2 PART MEASUREMENT AND TRANSFER

To automate a part transfer, it is necessary to locate the part and the receiving chuck in the same coordinate system. A touch probe is located with respect to the IC Chuck, which is used to hold the part while its inner contour is machined, as shown in Figure 1.

The touch probe then touches the part at three different points, which are used to determine the radius and center point of the hemisphere. The probe is referenced to radial and axial fiducial surfaces on the OC (outer contour) Chuck. The measurement will tell an operating computer whether the part is appropriately sized for the receiving chuck. It will also determine the position the part needs to be moved to for vacuum chuck transfer.

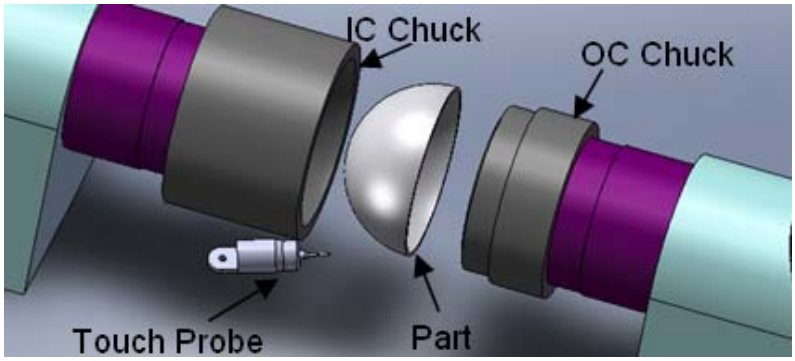

Figure 1: Exploded View of Hemishell Transfer

9.2.1 TRANSFER ERRORS

The probe touches used to locate and measure the part are accompanied by uncertainty. A calibration sphere was used to determine the trigger repeatability of a Renishaw TP6 touch probe. The trigger repeatability of 0.28 µm represents that the best possible accuracy of a calibrated probe measurement. Each point touched by the probe carries this error, which results in a 1.35 µm radius and 1.60 µm center-point uncertainty. Figure 2 shows how a 0.28 µm error at each of three touch points results in radius and center-point errors.

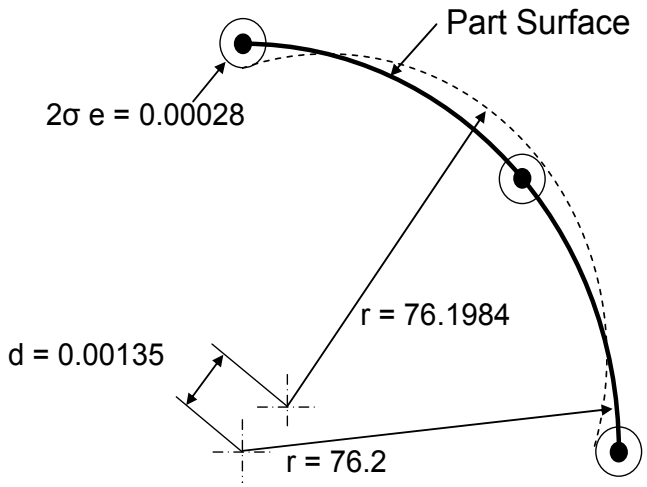

Figure 2: Measurement Errors Resulting From the Three-Point Method (mm)

9.2.2 TRANSFER DEMONSTRATION

A transfer was demonstrated on the PEC's ASG 2500 DTM. The part was effectively measured as described above. Variation in radial separation between the part and IC Chuck was less than 3

μm at transfer. Also, the part was located within 5 μm of the receiving chuck in the axial direction. Since the receiving chuck was cut 50 μm bigger than the part, these location errors are insignificant. However, radial run-out of ~50 μm resulted from the transfer.

9.3 REALIGNMENT WITH FRICTION

The radial run-out that occurs at the moment of transfer must be corrected so that the features on either side of the part will be aligned. For a part on a vacuum chuck this entails actuating the part against the force of friction.

Substantial work has been done to characterize the highly non-linear phenomenon of friction [1]. In the simplest models, friction force is computed as the product of a friction coefficient, μ, and normal force, N, as in Equation (1).

$$F_f = \mu N \tag{1}$$

In reality, friction force is much more complicated than this simple relation because the friction coefficient is not constant. For example, static friction is typically higher than dynamic or Coulomb friction. On small scales the transition between static and dynamic friction is of interest.

9.3.1 STRIBECK, COULOMB, AND VISCOUS FRICTION

Stribeck friction attempts to describe the behavior of the friction force as a function of velocity, particularly in the transition between static and dynamic friction. Figure 3 shows the different types of friction forcing phenomenon.

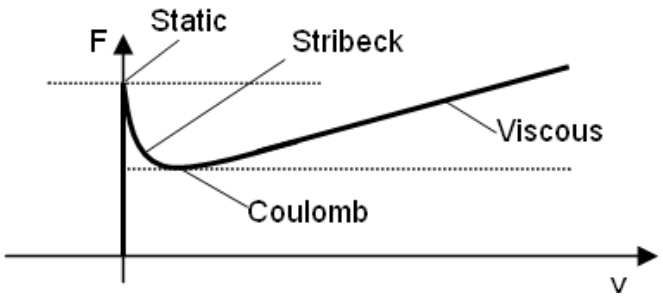

Figure 3: Combined Model of Friction Force as a Function of Velocity

For the purpose of precision part alignment, the relative velocity between the two sliding surfaces—the part and the vacuum chuck face—is small (~10 mm/s). As a result, the effects of viscous friction can be ignored.

9.3.2 STICK-SLIP BEHAVIOR

Stick-slip behavior results when a part is pushed across a friction interface by an actuator with some compliance, as diagramed in Figure 4.

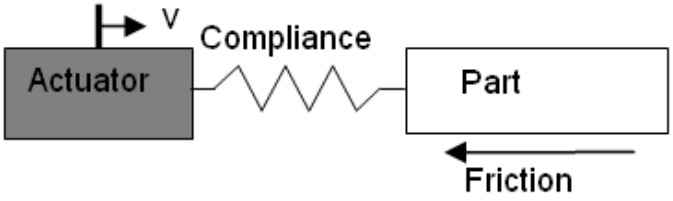

Figure 4: Stick-Slip Model Diagram

As the actuator moves towards the part at a constant velocity, the spring compresses and the force the actuator exerts increases linearly. As long as this force is less than the static friction limit, the friction force increases to exactly counter the spring force. Once the static friction limit is reached, the part begins to move. Then the friction force decreases rapidly, as described by Stribeck friction, and Equation (2).

$$F(v) = N\left(\frac{A}{\exp(bv)} + B\right) \tag{2}$$

Where A is the difference between the static and dynamic friction coefficients, B is the dynamic friction coefficient, and b is a chosen constant representing the rate of decay of the Stribeck friction curve.

The built up spring force propels the part ahead until eventually friction can slow and stop the part completely. The resulting behavior is described as stick-slip.

9.3.3 FRICTION INTERFACE MEASUREMENTS

The effects of Stribeck and Coulomb friction were measured. An aluminum puck was placed on a vacuum chuck and pushed with a load cell mounted to a DTM machining axis. The positions of the DTM axis and test puck were measured with electronic gages. These positions as well as the measured actuation force are plotted in Figure 5. It is clear from Figure 3 that the friction force drops when the test puck starts slipping. This effect results in "stick-slip" behavior, which is an impediment for precision control and must be considered in designing the positioning actuator.

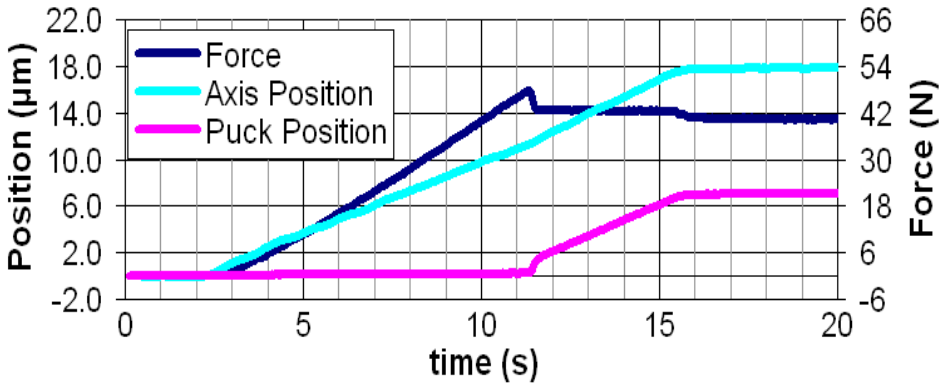

Figure 5: Measured Behavior of the Friction Interface

9.4 ACTUATION METHOD

A number of methods were considered to overcome the friction force holding a part on a vacuum chuck. The chosen method should be the one that satisfies the following criteria:

- Best position control
- Most repeatable
- Lowest risk of part damage
- Fastest realignment
- Easiest to implement

The methods considered included pushing the part with one of the machine axes, tapping the part to mimic the process currently used by skilled operators, vibrating the chuck in an attempt to reduce the friction coefficient and pulsing the vacuum to reduce the normal force.

9.4.1 TAPPING AS AN ACTUATION METHOD

For any actuation method, moving the part will require applying a force that is greater than static friction. However, once the part starts to slip and the friction force decreases, the part will accelerate rapidly under the same applied actuation force. Therefore, the best positioning control will likely come from force that exceeds the static friction limit for a short period of time before being removed. This forcing behavior is best realized with a tap, which has a force profile like those shown in Figure 6.

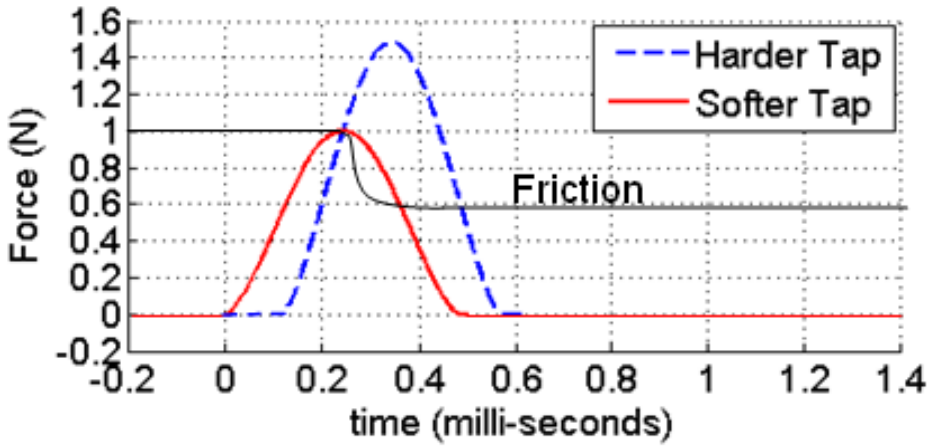

Figure 6: Force Profiles of Hammer Taps and Friction

Once a tap force exceeds the static friction limit, the friction force will drop and the difference between the input tap force and the retarding friction force will accelerate the part. The area between the tap force profile and the friction force profile is proportional to the momentum imparted on the part. Even when the peak of the tap force barely exceeds the static friction limit, as in the case of the solid line in Figure 6, there is a non-zero amount of work done on the part. This suggests that there is a minimum distance a part can be moved against the non-linear friction force.

9.4.2 TAPPER DESIGN AND IMPACT MODELING

An actuator has been designed to apply a peak force of 250 N (56 lbs) to a part without damaging it. An aluminum part has been assumed in the analysis. The tapper is designed based on the impact dynamics, which result from the Hertzian deflection of the plunger head and the part.

Hertzian Deflection

The Hertzian deflection of the tapper head and the aluminum part surface causes a tap to produce force a profile similar to those in Figure 4. The deflection of the impacting bodies allows the collision to take place over a finite, non-zero time, thus preventing damaging force spikes. The behavior of the two impacting spheres during a tap can be related by equations for elastic deformation [2].

As a Hertzian impact progresses, the centers of the two impacting spheres approach each other and the force between them builds according to Equation (3).

$$P = \left(\frac{y}{1.040}\right)^{\frac{3}{2}} \left(\frac{K_D}{C_E{}^2}\right)^{\frac{1}{2}} \tag{3}$$

where C_E and K_D relate to the material properties and diameters of the two impacting bodies via:

$$C_E = \frac{1-\nu_1{}^2}{E_1} + \frac{1-\nu_2{}^2}{E_2} \text{ and } K_D = \frac{D_1 D_2}{D_1 + D_2} \tag{4}$$

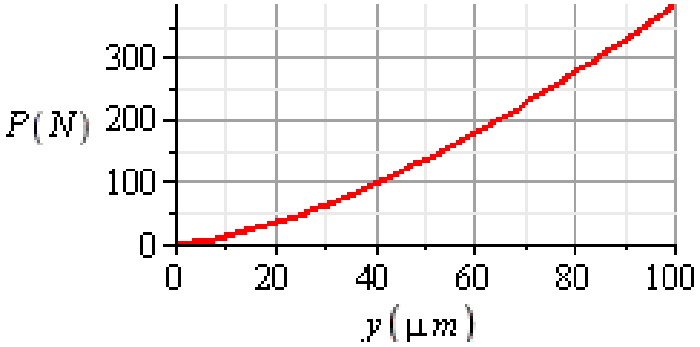

Figure 7: Variation of Impact Stroke with Applied Force

Figure 7 shows that an impact stroke of about 75 µm (0.003") will develop a peak force of 250 N (56 lbs). At the moment the impact starts, the approach of the center-points of the two impacting bodies, y, is zero. As the impact progresses the force that the actuator is exerting on the part increases. The initial kinetic energy of the actuator's moving element required to generate an impact stroke of 75 µm and peak force of 250 N can be found via Equation (5):

$$E_0 = \int_{y=0}^{y=75} P(y)dy \tag{5}$$

Equation (5) represents the area under the curve in Figure 7. The integral is solved below:

$$E_0 = \int_{y_0}^{y_f} \left(\frac{y}{1.040}\right)^{\frac{3}{2}} * \left(\frac{K_D}{C_E{}^2}\right)^{\frac{1}{2}} dy \Rightarrow \frac{2}{5*1.040} * \left(\frac{K_D}{C_E{}^2}\right)^{\frac{1}{2}} y^{\frac{5}{2}} \Bigg|_{y_0}^{y_f} \tag{6}$$

Solving with y_0 equal to zero and substituting in Equation (3) for y, Equation (5) can be solved for the initial kinetic energy required to produce a peak impact force, P.

$$E_0 = \frac{2*1.040^{\frac{3}{2}}}{5} \frac{C_E^{\frac{2}{3}}}{K_D^{\frac{1}{3}}} P^{\frac{5}{3}} \tag{7}$$

Equation (7) is plotted in Figure 8.

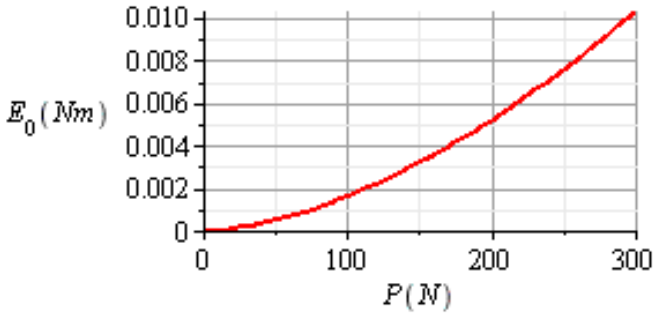

Figure 8: Initial Kinetic Energy, E_0, Required to Produce Peak Force, P

An initial kinetic energy of 0.00763 Nm is required to produce a peak force of 250 N (56 lbs).

9.4.3 ACTUATION SIMULATION

A friction model is combined with the impact model to simulate the response of a part on a vacuum chuck to a controlled tap. The simulations below show the displacement of an aluminum hemishell part with an outer radius of 76.2 mm and inner radius of 69.9 mm. The simulations are run with an initial energy of 0.009 Nm. The static friction coefficient is taken as 0.25, the dynamic friction coefficient as 0.15, and the normal force from vacuum is 1000 N.

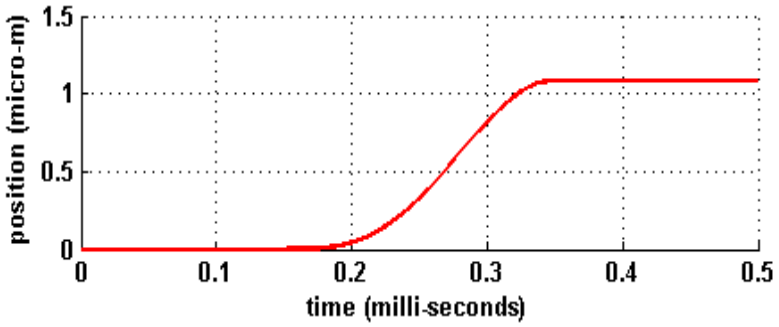

Figure 9: Part Displacement Due to Impact

Figure 9 shows that the part begins to accelerate at 0.15 ms, immediately after the impact force exceeds the friction force.

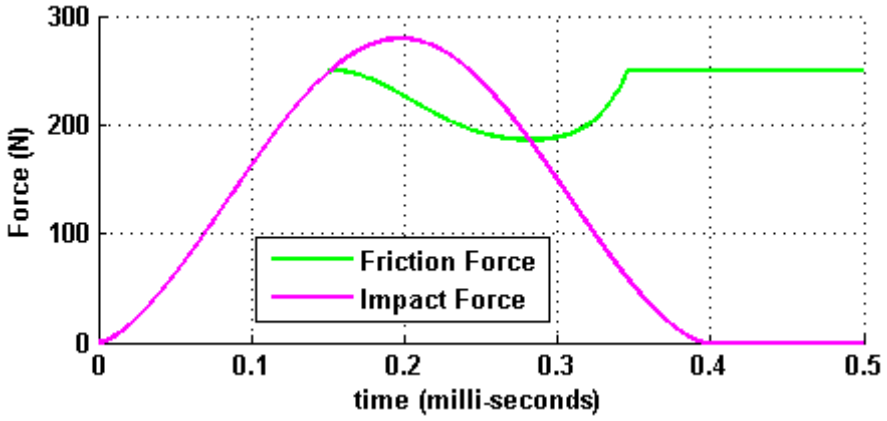

Figure 10: Simulated Actuation Forces

Figure 10 shows how the motion of the part reduces the friction force. The area between the friction force and impact force lines in Figure 10 is equal to the momentum transferred to the part. This model predicts the permanent slip motion of a part due to an applied impact; it will be verified and calibrated in system testing.

9.4.4 Actuator Design

An actuator with a voice coil motor (VCM) has been designed to accelerate a translating core to the desired impact velocity then hold the core at that velocity until it impacts the part and produces the desired actuation force profile. The core travels on a linear ball bushing, as shown in Figure 11.

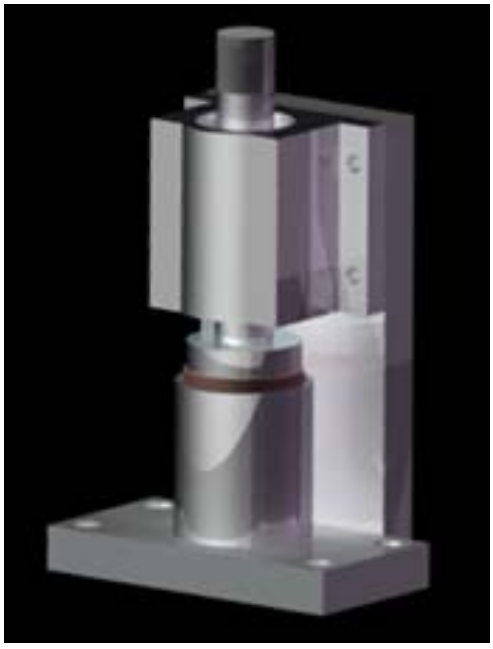

Figure 11: Model of Tapping Actuator

9.4.5 Actuator Performance

The realignment actuator was fabricated as planned. It was tested in the setup in Figure 12. A load cell was used to measure the peak impact force that resulted from a given impact.

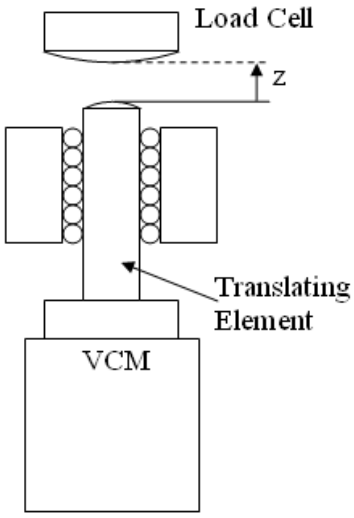

Figure 12: Test Setup for Voice Coil Motor Actuator

The impact was generated by the collision between the translating element of the VCM actuator and a stationary load cell. The VCM is driven with the waveform in Figure 13. The high voltage step is used to accelerate the sliding element, while the low voltage step is used hold the element at a constant velocity against gravity and viscous friction within the ball bushing. This input is multiplied by a gain to control peak force. If frequency is increased, the duty cycle is also increased proportionately.

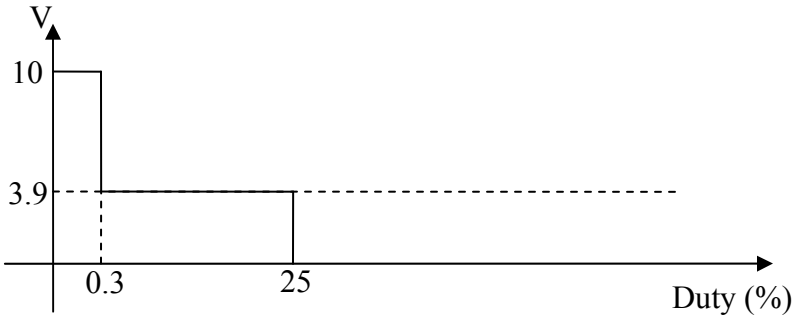

Figure 13: Voltage Input for VCM Actuator at 1 Hz

The load cell was tapped at while located at 6 different z-positions using 6 different frequencies. At each position and frequency, the cell was tapped 10 times, and the average value plotted in Figure 14 and Figure 15. The repeatability is quantified by the standard deviation—the largest standard deviation of peak impact force all of the data points taken was less than 1 N.

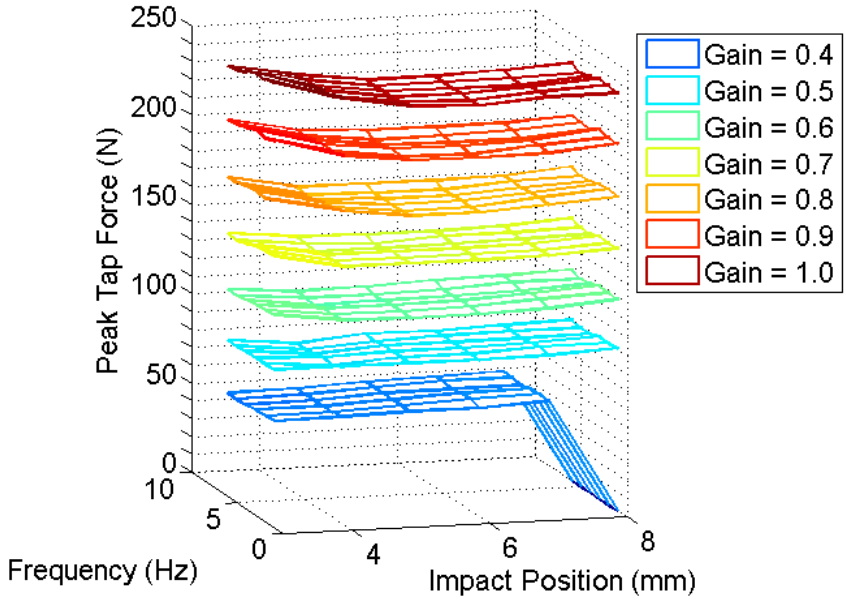

Figure 14: Peak Impact Force Variation with Operating Conditions

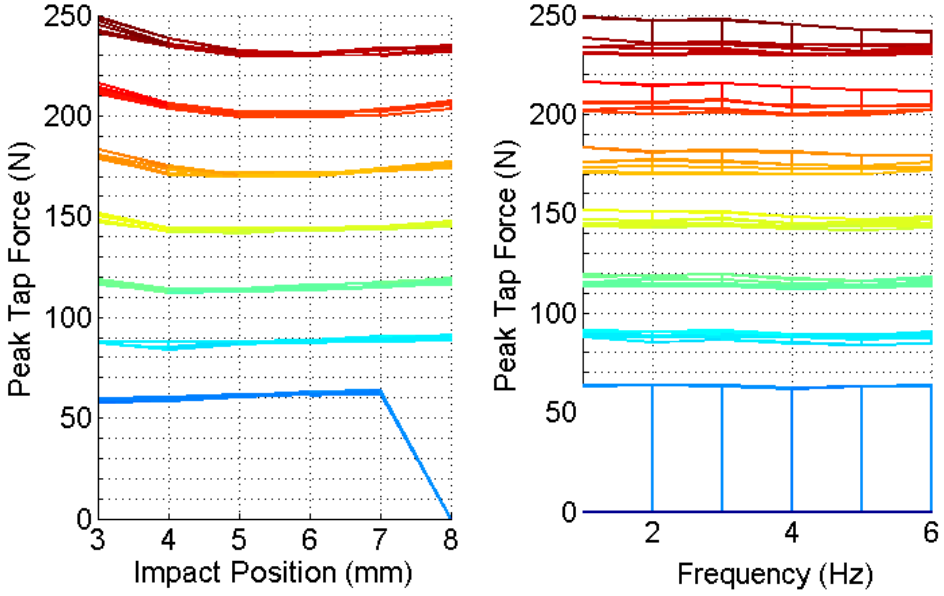

Figure 15: Peak Impact Force Variation

Tests on the VCM-based tapping actuator show that there is a range of 3 mm of stroke where the peak force variation is less than 7 N. Also, variation in operating frequency between 1 and 6 Hz does not greatly affect performance. Since the uncertainty (2σ) of each tap is less than 2 N the VCM actuator can produce a peak force with ±5.5 N uncertainty over a range of 3 mm. This

will allow the actuator to realign a part with 3 mm of run-out. In future work, the effect of this impact force variation on the incremental displacement of a part will be explored.

9.5 SUMMARY AND FUTURE WORK

A complete part transfer has been developed and demonstrated. The variation in radial separation between a the part and IC Chuck can be maintained to less than 3 μm, and the axial position of the part with respect to the chuck can be controlled to within 5 μm. During the transfer demonstration, radial run-out was observed as expected. An actuator has been developed that is capable of correcting misalignments of up to 3 mm. The number of run-out measurement and alignment iterations needed to center the part to within 5 μm will be determined in future work.

Also, an actuator has been designed and fabricated. Preliminary tests show that the actuator has a 3 mm range of stroke where the peak impact force has an uncertainty of 5.5 N. This uncertainty in the force input will contribute to uncertainty in the incremental displacement of a hemispherical part that is being actuated by the VCM tapper. This affect will be studied in future work. In finality, a given input signal will be correlated to a part displacement plus an uncertainty. The actuator will then be used in a complete system demo, which includes automated transfer, run-out measurement, and realignment.

REFERENCES

1. Olsson, H. et. al. "Friction Models and Friction Compensation." European Journal of Control (1998) 4: 176-195.
2. Roark, R., Young, C. K., "Formulas for Stress and Strain." McCraw Hill, 1975.